AD 749341

R-760/3-ARPA

June 1972

EFFECTS OF STRONG EXPLOSIONS - IV
(Soviet Literature Translations)

Compiled by Simon Kassel

A Report prepared for

ADVANCED RESEARCH PROJECTS AGENCY

Rand
SANTA MONICA, CA. 90406

90

DOCUMENT CONTROL DATA

1. ORIGINATING ACTIVITY	2a. REPORT SECURITY CLASSIFICATION
The Rand Corporation	UNCLASSIFIED
	2b. GROUP

3. REPORT TITLE

EFFECTS OF STRONG FXPLOSIONS - IV   (Soviet Literature Translations)

4. AUTHOR(S) (Last name, first name, initial)

Compiled by Kassel, Simon

5. REPORT DATE	6a. TOTAL NO. OF PAGES	6b. NO. OF REFS.
June 1972	89	

7. CONTRACT OR GRANT NO.	8. ORIGINATOR'S REPORT NO.
DAHC15 67 C 0141	R-760/3-ARPA

9a. AVAILABILITY/LIMITATION NOTICES	9b. SPONSORING AGENCY
DDC-A	Defense Advanced Research Projects Agency

10. ABSTRACT	11. KEY WORDS
English-language abstracts of 66 articles from Soviet technical literature on the effects of strong explosions, particularly nuclear explosions, and their simulation in the laboratory and in the field. The fourth in a series, this report covers articles mainly appearing in 1971 and early 1972. The abstracts are grouped under 13 headings, plus a miscellaneous category: (1) nuclear explosion effects, (2) explosions in various media, (3) shock waves in gases, (4) shock waves in liquids, (5) shock waves in solids, (6) flow past bodies, (7) ablation studies, (8) high-pressure effects, (9) electromagnetic field-plasma interaction, (10) ionospheric effects, (11) radiation damage, (12) laser effects on materials, and (13) mechano-electromagnetic effect.	Physics Lasers USSR--SCIENCE Thermodynamics Nuclear Explosions Details of illustrations in this document may be better studied on microfiche

R-760/3-ARPA

June 1972

EFFECTS OF STRONG EXPLOSIONS - IV
(Soviet Literature Translations)

Compiled by Simon Kassel

A Report prepared for

ADVANCED RESEARCH PROJECTS AGENCY

Rand
SANTA MONICA, CA. 90406

iija

PREFACE

This Report is one in a series entitled "Effects of Strong Explosions" and intended to provide an overview of current Soviet research activities in that field. It falls within the scope of a continuing program, sponsored by the Defense Advanced Research Projects Agency, which undertakes the systematic coverage of selected areas of Soviet scientific and technological literature.

The effects of strong explosions, particularly nuclear explosions, and their simulation under laboratory and field conditions involve a very broad range of phenomena and parameters such as high temperatures, pressures, electromagnetic energy densities, interaction of energy with materials, shock waves in gases, liquid, and solids, and, in general, events occurring under conditions of a high degree of mechanical, thermal, and radiation stress. The series of Rand Reports of which this is the fourth to be published will cover a variety of the pertinent topics as they are reflected in the currently available Soviet literature, by supplying abstracts from and summaries of the scientific and technological publications of the USSR.

The material in the present Report is derived exclusively from Soviet technical writings that, with a few exceptions, appeared in 1971 and the early part of 1972. The abstracts here included were prepared by Informatics, Inc. They have been arranged by the compiler according to fairly general subject areas, and vary in length depending on the pertinence and significance of the individual papers.

The information assembled in this Report covers our most recent knowledge of Soviet research on the effects of explosions, and should prove useful to American scientists working in this and related fields of research.

CONTENTS

Preceding page blank

KEY TO JOURNAL ABBREVIATIONS

AN MoldSSR	Academy of Sciences, Moldavian SSR
DAN BelSSR	Doklady Akademii Nauk Belorusskoy SSR (Reports of the Academy of Sciences of the Belorussian SSR)
DAN SSSR	Doklady Akademii Nauk SSSR (Reports of the Academy of Sciences, USSR)
ECM	Elektronnaya obrabotka materialov (Electronic processing of materials)
FGiV	Fizika goreniya i vzryva (Physics of combustion and explosion)
FIKhOM	Fizika i khimiya obrabotki materialov (Physics and chemistry of materials processing)
F-KhMM	Fiziko-khimicheskaya mekhanika materialov (Physico-chemical mechanics of materials)
FTT	Fizika tverdogo tela (Solid-state physics)
IAN Energ	Akademiya nauk SSR. Izvestiya. Energetika (Power engineering)
I-FZh	Inzhenerno-fizicheskiy zhurnal (Engineering physics journal)
IVUZ Fiz	Izvestiya vysshikh uchebnykh zavedeniy. Fizika (IVUZ, Physics)
MZhIG	Mekhanika zhidkosti i gaza (Mechanics of liquid and gas)
PM	Prikladnaya mekhanika (Applied mechanics)
PMM	Prikladnaya matematika i mekhanika (Applied mathematics and mechanics)
UFZh	Ukrainskiy fizicheskiy zhurnal (Ukrainian journal of physics)
ZhETF	Zhurnal eksperimental'noy i teoreticheskoy fiziki (Journal of experimental and theoretical physics)
ZhETF P	Zhurnal eksperimental'noy i teoreticheskoy fiziki, Pis'ma (Journal of experimental and theoretical physics, letters)

Preceding page blank

ZhPMTF   Zhurnal prikladnoy mekhaniki i tekhnicheskoy fiziki
(Journal of applied mechanics and technical physics)

ZhPS   Zhurnal prikladnoy spektroskopii (Journal of applied
spectroscopy)

ZhTF   Zhurnal tekhnicheskoy fiziki (Journal of technical
physics)

I. NUCLEAR EXPLOSION EFFECTS

Kukhtevich, V. I., I. V. Goryachev, and L. A.
Trykov. Zashchita ot pronikayushchey radiatsii
yadernogo vzryva (Protection against the penetrating
radiation of a nuclear explosion). Moscow, Atomizdat,
1970, 190 p.

An engineering design method is presented for the protection
of ground structures against the penetrating radiation of a nuclear explosion.
The book is based on Soviet and Western open source materials published in
1958-1969; Soviet sources make up about 50% of the 123 references.

Physical aspects of nuclear explosion are treated only briefly,
since they are covered well enough in several recent Soviet and Western mono-
graphs. Emphasis is placed on neutrons and gamma-rays produced at the
atmosphere - ground boundary and their penetration through a typical protective
shield. Numerous published data on characteristics of ionizing radiation are
assembled for use in the design of protection against nuclear radiation.

Formulas and numerical data are given for calculation of the
dose rate of primary gamma radiation propagating from a point source and
from a spherical radioactive cloud through an infinite atmospheric medium.
The effect of a shock wave created by an explosion on the propagation of
primary gamma-rays is evaluated in the cases of aerial and ground explosions.
Formulas are also given for the dose rates of primary and secondary gamma
-radiation with allowance for the shock wave effect, as well as the time,
explosive force, distance from the explosion center, and ascent velocity of
the radioactive cloud. Numerical values for an integral dose of gamma
radiation at a given distance from the explosion center are described by formulas
for low and high explosive forces, and plots of gamma-ray accumulation rate
versus time are shown. Theoretical data are included on: spatial distribution
of slow neutrons released by a nuclear explosion and formed in air by moder-
ation and diffusion of delayed neutrons; integral neutron albedo from the
ground surface and coefficients of the angular distribution function of scattered
neutrons; and characteristics of neutrons reflected from the ground by a
nuclear explosion in the atmosphere. Calculated data are also presented
on integral gamma-radiation albedo in a nuclear explosion.

Other tables give theoretical and experimental data on transmission
of nonscattered neutrons and total neutron dose through an iron shield of
varying thicknesses and at different angles of incidence; transmission of a
total dose of neutrons through water, polyethylene, and iron shields; trans-
mission of nonscattered neutrons from a nuclear reactor through an iron,

concrete, or polyethylene shield; and angular distribution of the dose rate of scattered neutrons beyond an iron or polyethylene shield. Experimental and theoretical data are plotted and tabulated on angular distribution (differential albedo) and integral albedo of neutrons back-scattered from water, ground, and iron at different neutron beam angles of incidence.

Theoretical mass coefficients of attenuation of nonscattered gamma-radiation by different materials are tabulated and discussed. Theoretical transmission coefficients of gamma-radiation scattered by iron shields of varying thicknesses and at different angles and characteristic angles of scattering for specific energies and materials are tabulated. Formulas used to calculate the tabulated data are given. Empirical formulas are cited for calculating integral energy albedo of gamma quanta back-scattered from protective shields. The approximate formula for bremsstrahlung energy of beta-electrons is given and data on the relative contribution of spectral components of bremsstrahlung were tabulated. Secondary gamma-radiation yield beyond the shield is analyzed, and the numerical values of the constants for calculation of the yield are tabulated for water, iron, and concrete. Calculated yield functions for different shield thicknesses are plotted.

Two methods of designing the protection of ground structures are outlined: (1) an exact method involving the use of computers and, (2) a simplified method using approximate formulas. Both methods require a knowledge of the barrier and geometry factors of radiation attenuation. The formulas for calculation of these factors are given, and the sequence of mathematical operations associated with the two methods is described. The precise method consists of six consecutive steps.

The effects are evaluated of the multiple scattering of radiation on the inner walls of a structure.

Appendices contain 8 tables of barrier factors of transmission of neutrons and gamma-radiation through various materials, and two tables for yields of trapped gamma-radiation for various materials.

Kozlov, V. I., and Yu. G. Shafer. On a possible mechanism for the localization of fission products from a high-altitude nuclear explosion. Kosmicheskiye issledovaniya, no. 4, 1971, 630-631.

Recorded particle data on the Cosmos 3, 5 and 6 satellites following the U. S. Starfish high-altitude detonation in July, 1962 showed a concentration of fission products at the conjugate point to Johnson Island.

This concentration was detected at high altitudes and persisted for an appreciable length of time. In the present paper the authors use the Starfish results for a model with which they analyze the type of trapped particles, their transport characteristics, and the geometry of the trap region at the conjugate point.

A magnetic-gravitational trap is postulated in the conjugate point region which will act as a potential well for the heavier charged particles. At some radial distance r_o from earth center the combination of gravity and repulsion potentials will have a minimum, which determines the depth of the potential well; in the proposed model this is shown to be $E_\perp = m g r/3$, where m = ion mass. Assuming particles with atomic weight of 100 and an altitude of 400 km, we find that $E_\perp \cong$ 30 ev, i.e., the portion of the dispersing cloud of fission products having energies on the order of 30 ev will be trapped at the 400 km level. This level is consistent with the values obtained by Neff et al [1] and Golgate [2] at the conjugate point.

The arrival time of the major portion of charged particles is generally a function of plasma dispersion in the geomagnetic disruption at the detonation point; Askar'yan [3] gives the velocity as on the order of 10^7 cm/sec for the Starfish test, which for a force line length of about 4×10^8 cm yields an arrival time of 40 seconds.

The authors next examine the factors determining the duration of the trap region. As the analysis shows, the size of the well is a direct function of particle charge, hence the well assumes a "funnel" configuration according to trapped charge level. The confinement time is given approximately by

$$\tau_c = 0.785 \times \tau_i \ln \frac{B_{max}}{B} \, ,$$

where τ_i is mean ion relaxation time and B is magnetic inductance, on the assumption that the main loss mechanism is coulomb scattering in the funnel region. If a Maxwellian temperature distribution of atmospheric ions is assumed, then a numerical solution for τ_c under the assumed atomic weight and ionization level falls in the range of 10^2--10^5 sec in the 250--1000 km altitude range. This suggests that the cone region is sustained by continuous replenishment of particles from the upper energy regions.

Finally, it is concluded that dissipation of the funnel region owing to drift of trapped particles is negligible (0.2 - 0.5 deg/day), which was corroborated by experimental evidence that the trap region acted as a compact β and γ radiation source for a substantial period.

References

1) Nef, C. G. et al. Operatsiya "Morskaya zvezda". Atomizdat, 1964, 109.
2) Golgate, S. A. J. Geophys. Res., v. 70, no. 13, 1965, 3161.
3) Askar'yan, G. A., and M. S. Rabinovich. ZhETF, v. 48, no. 1, 1965.

Shafer, Yu. G., V. I. Kozlov, I. S. Kiriyenko, A. D. Bolyunova, R. B. Salimzibarov, and S. M. Oshchepkov. Measurements of radiation effects of the thermonuclear explosion in China, December 27, 1968, by the Cosmos-259 and Cosmos-262 artificial satellites. Kosmicheskiye issledovaniya, no. 4, 1971, 558-564.

This paper is the first extensive analysis to appear of Soviet recordings of explosion products from the Chinese nuclear explosion in December, 1968. At the time of the explosion two Cosmos satellites were in orbit and carrying several types of radiation monitoring equipment: Cosmos-259 (apogee 1353, perigee 219 km), and Cosmos-262 (apogee 818, perigee 263 km). The orbital planes of both were inclined at 49° to the equatorial plane. The Cosmos-259 recording equipment included triple-coincidence panoramic telescopes featuring type STS-5 gas discharge counters (identified as the STS channel), and an unshielded STS-5 counter, identified as the SSVS channel, mounted on the end of a 2 meter boom. The panoramic system recorded only charged particles, protons with $E > 190$ MeV and electrons > 12.5 MeV; the single SSVS counter was intended for protons ≥ 10 MeV and electrons ≥ 50 KeV; it could also register photons, but at an efficiency not above 1%. The 262 carried an intensity array consisting of four STS-5 gas discharge counters connected in parallel and shielded by 3m Al and 3 mm Pb screens.

This equipment was used to transmit real-time data on radiation intensity levels from orbital regions over the USSR, Mongolia and China, around the time of the detonation. For the purpose of illustration the authors have chosen the intensity data from orbits lying below the regions of stable capture of near-earth radiation. This data is presented graphically according to satellite trajectory as shown in Figs. 1-3, giving increase in count rate N over that of a "quiet" day, i.e., December 18 and 19, 1968.

The data show that the shielded single counter (SSC) in the Cosmos-259 recorded during two minutes an ~80% increased intensity in its 196th orbit, i.e.,

about 10 hours after the explosion; this recording was made at an altitude of about 700 km over the Mongolian Peoples Republic in an area whose coordinates were 43-45°N. Lat. (geographic) and 100-110°E. Long. The counting rate of the triple-coincidence telescope increased at the same time. Twenty-four hours after the explosion, over approximately the same territory in the 209th and 210th orbits above the eastern territory of China, the satellites noted an increase of intensity $(\Delta N/N)_{SSC}$ = 20 and 60%, $(\Delta N/N)_{STS}$ = 50 and 40%, respectively. In the 211th orbit, the counting rate increments of the single shielded counter reached 1.5-2 pulses per second, which amounts to 30-40% over background.

On December 27 in the 196th orbit, beginning with 2113-2117 hours, the external SSVS counter rates increased by a factor of 2-8; a maximal increase by a factor of 10 was noted at 2115 hours 30 seconds. Subsequently the count rate began to fall off and at 2118 hours only background oscillation was recorded. In the 197th orbit, the count rate increased by a factor of 2-2.5. On December 28 in the 209th orbit, the satellite recorded only the cosmic ray background while in the 210th orbit, whose trajectory is near the 196th orbit, in a real-time transmission regime, the count rate increased by a factor of 1.5-2. The maximum "excess" of the count rate in the 211th orbit, whose trajectory almost coincided with the 197th orbit, reached 100%.

Analogous results are reported for the Cosmos-262 count rate, e.g., 262's counters registered a doubled intensity 23 hours after the explosion; the recording was also made over the Mongolian Peoples Republic in an area whose coordinates were 48-47°N. Lat. and 95-105°E. Long., at an altitude of 270 km.

It is noteworthy that no increase in radiation intensity was recorded when the Cosmos-259 satellite passed in its 209th orbit over the magnetic conjugate of the Chinese explosion point, which is to be expected in low altitude explosions. Consequently, there was no direct ejection of explosion products into the force tube. A further theoretical analysis is given to define the absorption mechanism taking place in the vicinity of the detonation point; the fact that neither Cosmos satellite intercepted fission fragments is taken as evidence of strong atmospheric absorption, and on this basis it is concluded that detonation occurred at not over 20 km altitude.

The level of protons above 190 MeV registered by the STS counters suggests that there may have been some release of them from the radiation belts owing to the disturbing effect of the Chinese detonation. Using calculations from the U. S. Starfish test, the authors verify this mechanism as a possible additional result of the test.
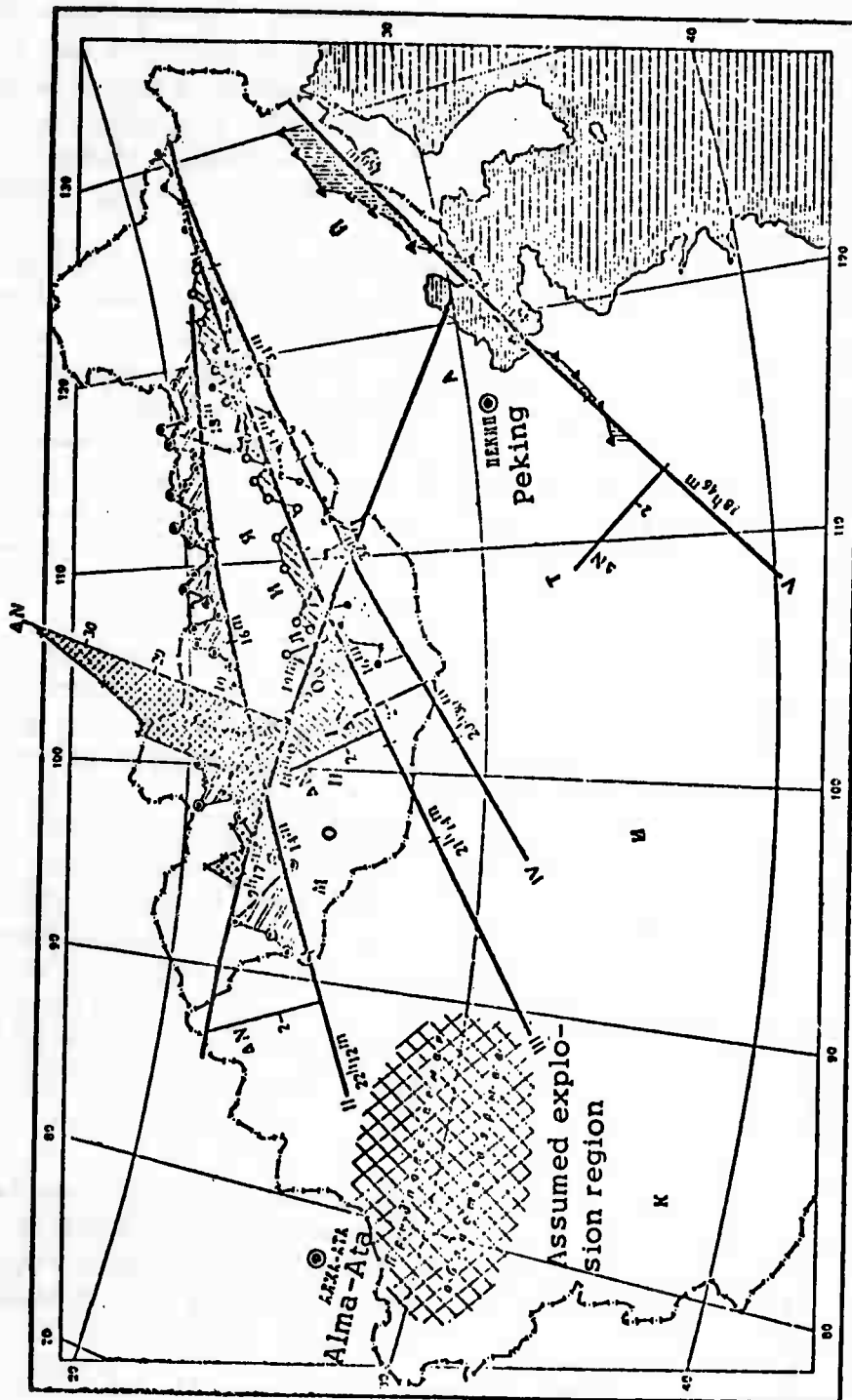
Fig. 1. Variation of radiation intensity from the Chinese thermo-nuclear explosion according to data of the single shielded counter (SSC). I -- 29th orbit, 12-28-1968, Kosmos-262; II -- 211th orbit, 12-18-1968, Kosmos-259; III -- 196th orbit, 12-27-1968, Kosmos-259; IV -- 210th orbit, 12-28-1968, Kosmos-259; V -- 209th orbit, 12-28-1968, Kosmos-259.
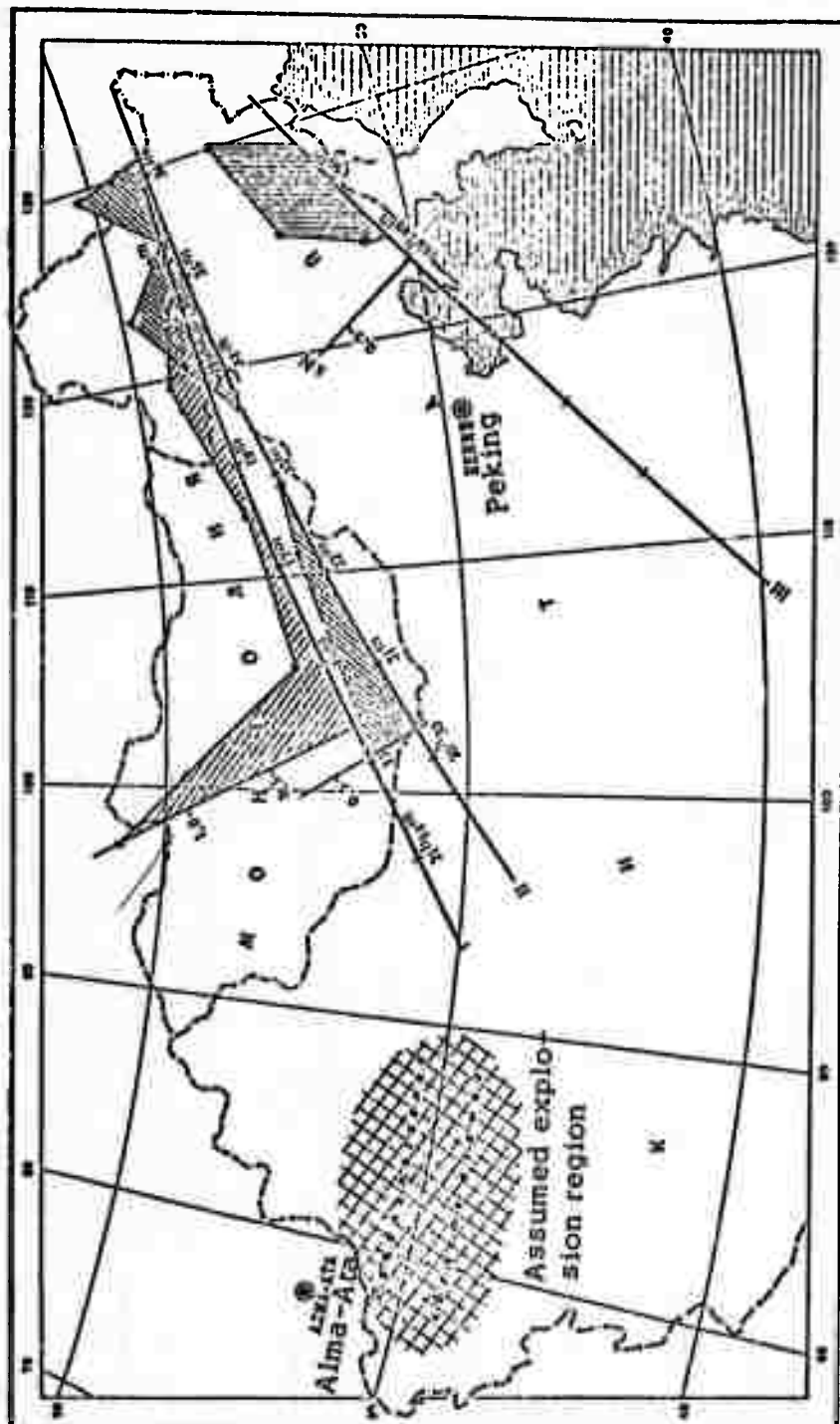
Fig. 2. Variation of radiation intensity from the Chinese ther-
monuclear explosion according to data from the panoramic
triple-coincidence telescopes (STS) on board Kosmos-259.
I -- 196th orbit, 12-27-1968; II -- 210th orbit, 12-28-1968;
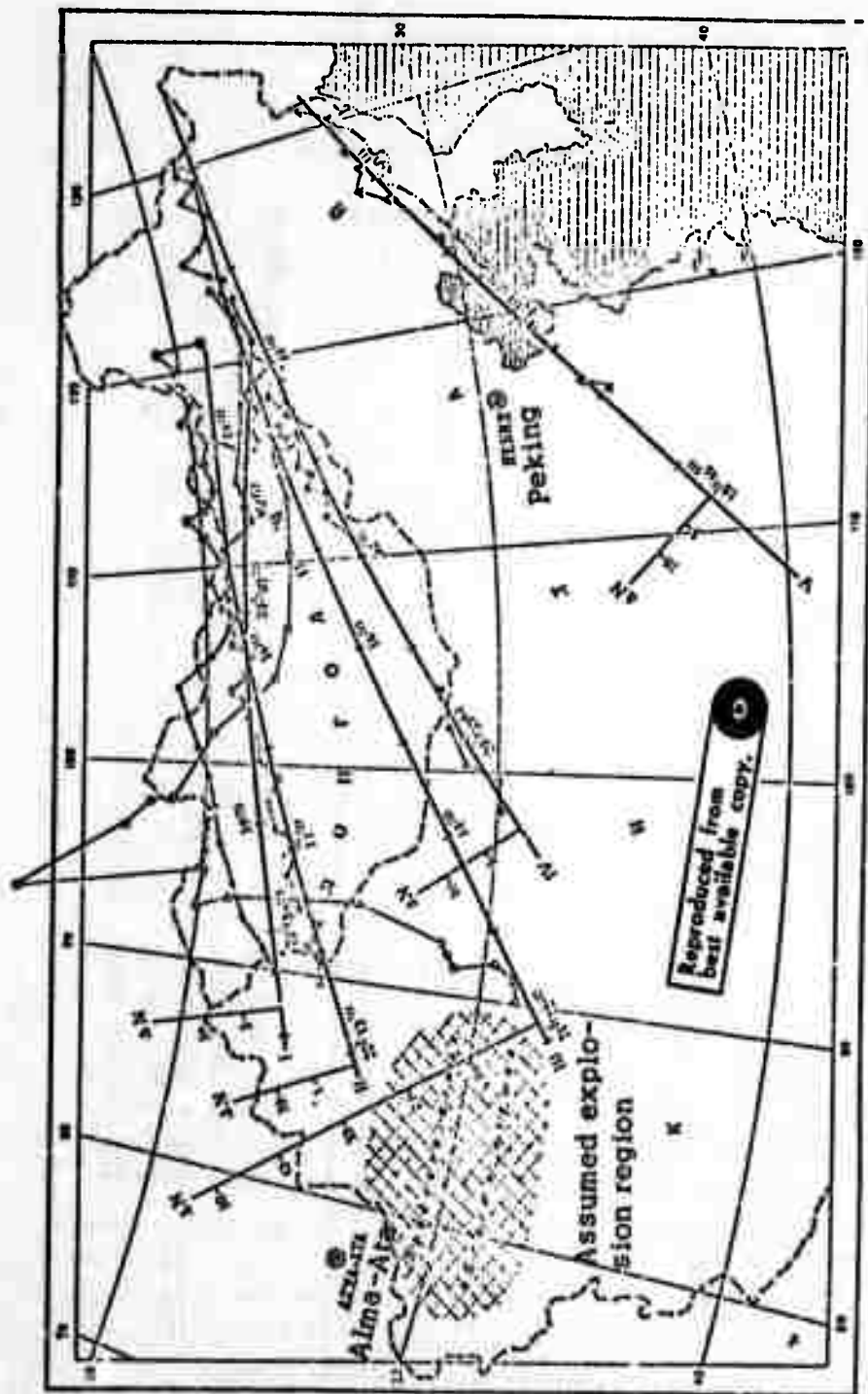III - 209th orbit, 12-28-1968.

Fig. 3. Variation of radiation intensity from the Chinese thermonuclear explosion according to data from the SSVS external counter on board Kosmos-259. I -- 197th orbit, 12-27-1968; II -- 211th orbit, 12-28-1968; III -- 196th orbit, 12-27-1968; IV -- 210th orbit, 12-28-1968; V -- 209th orbit, 12-28-1968.

II. EXPLOSIONS IN VARIOUS MEDIA

Rodionov, V. N., and A. P. Sukhotin.
Parameters of elastic waves generated by a
spherical explosion in metals of different
strength. FGiV, no. 1, 1971, 142-146.

An experimental study was made of the effect of yield point σ
in uniaxial elongation of A-00 aluminum (1), D-16 annealed (2), and D-16
hardened duralumin (3) on the parameters of an elastic compression wave
generated by a 0.2 g spherical charge of TEN. A diagram of the experiment
is shown in Fig. 1. The metal samples had similar mechanical characteristics,
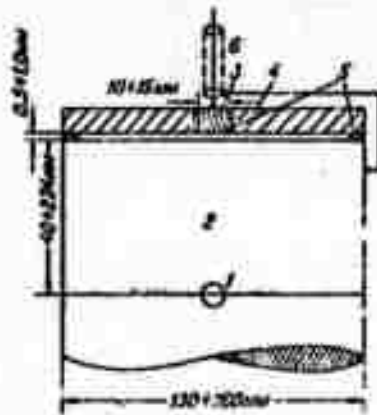

Fig. 1. Experimental setup: 1 - explosive
charge; 2 - metal block; 3 - pickup plate;
4 - guard ring; 5 - insulators; 6 - cable.

with the exception of differences in strength. The measured σ was 450,
1600, and 3000 kg/cm for samples (1), (2) and (3). Velocity rise time
τ_1, positive phase duration τ_2, and maximum mass velocity U_m were
measured on oscilloscope traces of free metal surface displacement. The
experimental plots $\tau_1 (r)$, $\tau_2 (r)$, (Fig. 2), and $\lg U_m(\lg r)$ indicate that
elastic waves are generated by the explosion, and the observed differences
in temporal wave parameters are the effect of strength only. This effect
was also evident in variations between the measured volume of the explosion
cavities of the three metal samples (1.3, 0.75, and 0.42 cu cm, respectively).
The linearity of the calculated plots of the relative maximum mass velocity
versus distance from the explosion center confirms that the extent of plastic
deformation is determined by the static σ of the metal. The motion
pattern and state of the metal in the elastic region was reconstructed
from the experimental data and the equation of plasticity. The effect
of σ on the motion of the boundary line R_* at which the difference of
principal stress is equal to σ of the metal is shown in Fig. 3. An increase
in σ affects both the amplitude and temporal parameters of R_* motion.
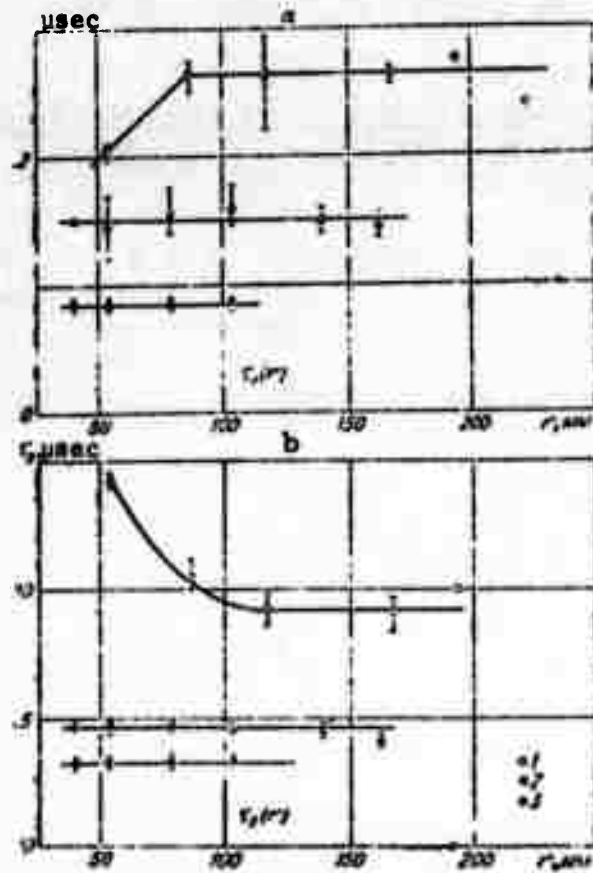
Fig. 2. Velocity rise time (a) and positive
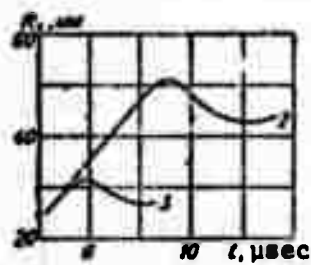phase duration (b) versus distance r from
the explosion center.

Fig. 3. The effect of σ of the 2 and 3
metals on boundary line R_*

An explosion in a quartz-like medium was calculated on a computer using a RAND (rashet adiabaticheskikh nestatsionarnykh dvizheniy) program for nonstationary adiabatic motion. The program takes into account the polymorphic phase transition of quartz into "stishovit". A two-liquid model was adopted for the medium with a gas bubble in its center; high pressure expansion of the bubble simulated a point explosion. In the region of continuous flow, pressure P and internal energy E of each phase were calculated from the equations

$$dE + P \, dV = 0, \tag{1}$$

$$P = P_x(\rho) + \Gamma \rho (E - E_x) \tag{2}$$

where $\quad P_x = \dfrac{\rho_0 c_0^2}{n}(\delta^n - 1), \quad E_x = \dfrac{c_0^2}{n}\left[\dfrac{\delta^{n-1} - n}{n-1} + \dfrac{1}{\delta}\right] + E_0, \quad \delta = \rho/\rho_0 = 0.605,$

$n_1 = 4$, $n_2 = 2.7$, $\Gamma_1 = \Gamma_2 = 0.55$, E_0 = const. P, V, and E were correlated by a $P = P(T)$ equilibrium curve and the equation of state of the mixture,

$$E - E_* = [T \, dP(T)/dT - P(T)](V - V_*)$$

where V_* and E_* are, respectively, specific volume and internal energy of one of the phases along the equilibrium curve. In many cases, expansion shock and bifurcated compression waves appear at the phase mixture boundary. Allowance was made in the RAND program for these waves. The calculated shock wave parameters were plotted against a dimensionless variable $\bar{r} = r/r_g$, where $r_g = \left[Q/(\rho_0 C_0^2)\right]^{1/3}$ (Fig. 1). The plots show that P and U
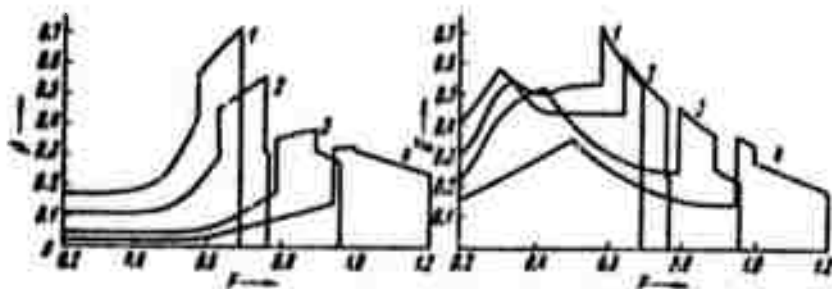

Fig. 1. Dimensionless pressure P and velocity $\bar{U}$ versus time: 1 - before bifuration of the first shock wave; 2, 3, and 4 - after bifuration.

behind the first shock wavefront increase significantly before dropping stepwise at the front of the expansion shock wave.

Shurshalov, L. V. Calculation of powerful underwater explosions. MZhiG, no. 5, 1971, 36-40.

A problem on powerful underwater explosions is solved by finite-difference equations, with the introduction of an artificial viscosity $Q = Q_1 + Q_2$, where Q_1 and Q_2 are linear and quadratic components of Q. In contrast to relatively weak explosions, a full thermodynamic description of the properties of water over a broad range of pressures, temperatures and densities is required in the present problem. A numerical solution is developed using an equation of state derived earlier by the author (MZhiG, no. 4, 1967, 184) to describe the properties of water at pressures over 1,000 atm. At a pressure below 1,000 atm, the Tait equation of state was used.

A spherical envelope (v = 3) containing a strongly heated compressed gas and located in an infinite space filled with water, with specific volume V_2 at a pressure p_1, served as a mathematical model of an underwater explosive charge. Motion of water and gas was calculated from the time t = 0, when the envelope disappears instantaneously. A set of Lagrangian equations of motion, which included the term Q, and equations of state of detonation products and water were solved by the finite-difference method. A numerical calculation using the finite-difference equations was performed for explosion of a spherical TNT charge of $\rho_0 = 1.5$ g/cm^3 at about 60 m depth. Characteristic values selected were: $p_* = 10^4$ kg/m^2, $V_* = 10^{-2}$ m^4/kg x sec^2, and $l_* = r_0$, where r_0 is the initial radius of the charge. The coefficients C_1 and C_2 in the expressions $Q_1 = C_1 a \, \Delta U/V$ and $Q_2 = C_2^2 \, \Delta U^2/V$ (where $\Delta U = U(R + \Delta R)$-UR, U, V, and R are dimensionless velocity, specific volume, and Euler coordinate respectively, and a is the local sound velocity) were assumed to be $C_1 = 0.5$ for extremely powerful or ≈ 0 for weak waves and $C_2 = 2$. The calculated hydrodynamic parameters are plotted in Fig. 1-3, where $\tau = t/t_*$, dashed lines describe variations of the shock wave parameters, and $R_1 = 1$ corresponds to the boundary of a gas bubble. The dots and circles represent the data calculated with a time step twice (dots) and one half (circles) that used in calculation of data represented by the curves. Comparative analysis shows that the calculations are satisfactorily accurate. The flow parameters were also calculated for dispersion in water of a spherical (v = 3), cylindrical (v = 2), or a plane-parallel (v = 1) volume of a compressed gas whose initial parameters were $P_g = 5 \times 10^5$, $V_g = 0.49$, and $U_g = 0$.
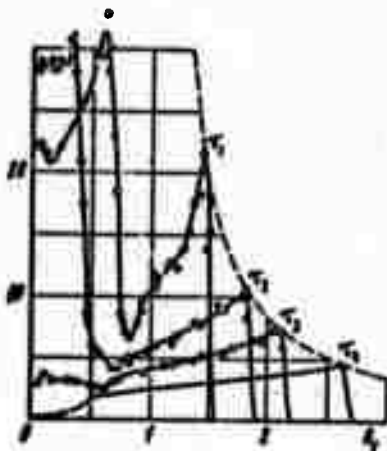
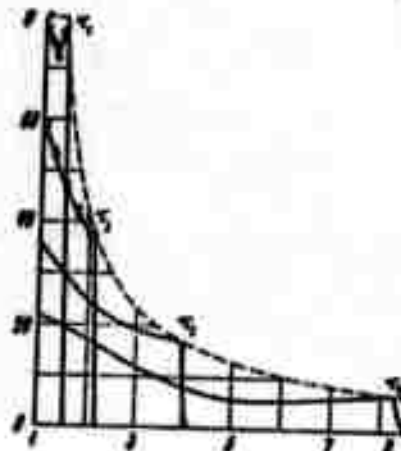Fig. 1. Pressure versus
Lagrangian coordinate R_1.
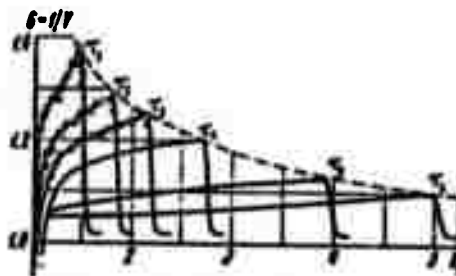
Fig. 2. Velocity versus
R_1.

Fig. 3. Density versus R_1.

In Fig. 4, calculated pressure, velocity, and density drop at the shock wave
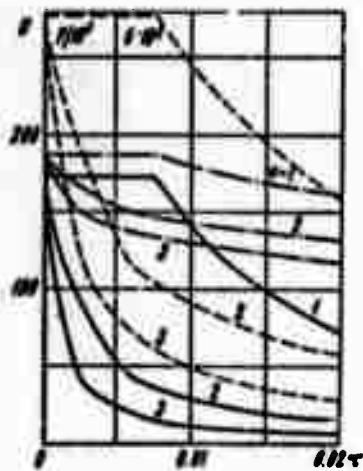front are plotted as continuous, dashed, and dot-dash lines.

Fig. 4. Shock wave parameters in water
versus time τ for $v = 1$, 2, and 3.

Simonov, V. A. On processes originating during
the falling of an impact wave on a tapered cavity.
FGiV, no. 2, 1971, 280-284.

Results are described of experimental investigations on processes
arising from an impact wave of subsonic velocity on the tip of a tapered cavity
in metals, and a study is made of the stability of the flat cumulation jet which
is produced. Experiments were conducted with aluminum, copper and steel,
the arrangement for which is shown in Fig. 1. The cylindrical explosive charge
of diameter 40 cm and height 10-15 mm consisted of type TG 50/50 compound.
Detonation of the charge was synchronized with photographic instruments to
obtain a true picture of the detonation processes; the range of angle γ(Fig. 1)
was varied from 0.5° to 32°.

Experiments with aluminum specimens showed that a flat cumulation
metallic jet was formed during the normal interaction of the impact wave on a
tapered cavity with an angle $2\gamma = 30°$. With decrease of γ, jet formation disappears,
that is, a regime of collapsing without jet formation occurs, characterized by
a periodic deformation very similar to wave formation during explosion welding.
The length of this wave was found to vary with change in angle γ. At $\gamma = 1.5°$,
wavelength λ was 1.5 mm; at $\gamma = 6.5°$, $\lambda = 5.5$ mm. In the range $\gamma \approx 6° \sim 8°$, both
wave and jet regimes were found to exist simultaneously. At $\gamma \geq 8°$, only the
jet regime existed, and at $\gamma = 15°$, this jet was capable of piercing through a
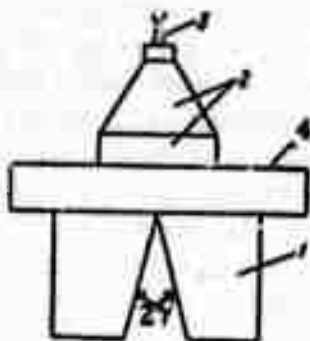duralumin plate of 10 mm thickness.

Fig. 1. Experimental sketch.
1 - metallic specimen; 2 - HE charge
with flat wave regenerator; 3 - detonator;
4 - metallic plate of given thickness.

A series of experiments with copper samples showed a very
similar process to that with Al, and the transition of wave regime to jet regime
was noted between the same interval of angles $\gamma = 6^\circ \sim 8^\circ$. The wavelength of
a Cu sample with respect to γ is given below. Increasing γ from 2° to 5° increases

γ°	2	4	5	5.5	6	7
$\lambda, \mu\mu$	1	2	2.5	3	3.5	3.5

wavelength from 1 to 3.5 mm; however a further increase in angle does not
increase the wavelength. It is noted that geometrical dissymmetry does not
affect the angle of transition from wave to jet formation, and that the jet formed
is always directed along the bisector of angle 2γ (Fig. 1).

Similar experiments with steel samples showed that transition of
wave to jet regime takes place at an interval between angles $\gamma = 4^\circ \sim 5^\circ$.

Experiments were also conducted with samples of different
materials, but having a like geometry. The angle of transition from wave to
jet regime was noted to increase very significantly. When one cube was titanium
and the other copper, the jet regime was noted only at angles $\gamma > 20^\circ$; and the
jet was inclined from the symmetrical axis towards the metal having a heavier
density, in this case copper.

The author makes a comparison of his results with those of Walsh
et al, (Mekhanika. Sbornik perevodov, vyp. 2(24), 1954), but they do not seem
to be in good agreement. In Walsh et al, angles of transition from wave to jet
formation for steel and Al were found to be $2\gamma = 30^\circ$ and $2\gamma = 34^\circ$, respectively,

taking into consideration the effects of incoming flow U_O. In the present article, U_O is neglected, as it depends very little on angle γ. ($U_O = \dfrac{D - U}{\cos \gamma}$, where D - velocity of impact wave in sample, U - body velocity of particles). According to Walsh et al, impact of solid bodies without jet formation has been proven possible, and it was established that jet formation cannot take place in presence of two impact waves at the point of contact. In the present article, the author points out that a stationary impact wave cannot exist at the point of contact at any angle γ, as the falling impact wave is at subsonic speed, so that the jet formation automatically occurs. However, in spite of the above discrepancies, the author still agrees with the possibility of the process occurring without jet formation, but with generation of deformations in the form of waves on the collapsing surface. He points out that in such a case, for explaining the phenomenon of transition from jet to wave regime, it is necessary to take into account other criteria related to the model of an ideal fluid.

III. SHOCK WAVES IN GASES

Pogorelov, V. I. The impact of an incalculable
supersonic jet on a plane. IFZh, v. 21, no. 5,
1971, 941-942.

Shock wave separation occurs in front of a plane positioned
normally to the nozzle axis when an incalculable supersonic jet impinges on
the plane. The separated wave is convex toward the plane and interacts with
the hanging shock of the jet if the nozzle-to-plane spacing is such that the
separated wave interferes with the expansion of a free jet. A flow measure-
ment equation is established for gas flow ahead of and behind the separated
shock wave with allowance for a relationship in the shock wave and on
assumption that the density and the velocity component parallel to the plane
are constant behind the separated wave. This flow equation is used to
derive a differential equation which defines the geometry of the generatrix
of the separated wave. The boundary condition of this equation is the derivative
of the shock wave equation for a triple configuration of shock waves. The
coordinate of the triple configuration is determined by a simple alg braic
correlation using the numerical value of the derivative. Gasdynamic parameters
of subsonic flow behind the shock wave can be also determined, if the relative
position versus the plane and the shape of the shock wave are known. The
calculated coordinates of the triple point and geometry of the separated shock
wave were found to be in good agreement with experimental data obtained
from flow shadow photographs.

Pustovalov, V. K. Self-similar gas motion
behind a shock wave front sustained by radiation.
DAN BelSSR, v. 15, no. 12, 1971, 1079 1081.

Adiabatic expansion of a cold perfect gas in vacuum, initiated
by a strong shock wave, is analyzed with allowance for radiant energy q
supplied to ($q > 0$) or withdrawn from ($q < 0$) the expanding gas. Shock wave
propagation through the gas is sustained by radiation which determines the
motion pattern of the shock front. The radiation flux density is defined by
$q = q_0 t^l$, where l is an integer. This is a self-similar gasdynamic problem
of the first kind, since there are two independent dimensional parameters
q_0 and ρ_0. The problem is described by the set of equations

$$\frac{d\rho_1}{d\xi}(v_1 - \xi) + \rho_1 \frac{dv_1}{d\xi} = 0,$$

$$\frac{k}{\alpha} v_1 + \frac{dv_1}{d\xi}(v_1 - \xi) + \frac{1}{\rho_1}\frac{dp_1}{d\xi} = 0,$$

$$-\frac{m}{\alpha} p_1 + \frac{dp_1}{d\xi}(v_1 - \xi) - \gamma \frac{p_1}{\rho_1}\frac{d\rho_1}{d\xi}(v_1 - \xi) = 0 \qquad (1)$$

where ρ_1, p_1, v_1 are the unknown dimensionless density, pressure, and velocity of the gas, ξ is a self-similar variable, γ is the adiabatic exponent, $\alpha = 1 + \ell/3$ is the self-similarity index, $k = \ell/3$, and $m = 2\ell/3$. The boundary conditions at the shock front and on the vacuum side complete the formulation of the problem.

Solution of (1) with the boundary conditions is given as follows:

$$p_1 = A_1 \left(-\frac{1}{2(2-\gamma)} + \frac{\gamma-1}{2-\gamma}\xi\right)^{\frac{\gamma-2}{\gamma-1}}$$

$$\rho_1 = B\left(-\frac{1}{2(2-\gamma)} + \frac{\gamma-1}{2-\gamma}\xi\right)^{-\frac{1}{\gamma-1}}$$

$$v_1 = \frac{1}{2-\gamma}\left(-\frac{1}{2} + \xi\right) \qquad (2)$$

$$A_1 = \frac{1}{4-2\gamma}\left(\frac{2\gamma-3}{4-2\gamma}\right)^{\frac{2-\gamma}{\gamma-1}}, \quad B = -\left(\frac{2\gamma-3}{4-2\gamma}\right)^{\frac{2-\gamma}{\gamma-1}}$$

$$a = \frac{7-5\gamma}{8(2-\gamma)^2(\gamma-1)} \qquad (3)$$

where a is one of the dimensionless constants which define the boundary condition at the shock front. Solution (2) for $a = 0$ and $\gamma = 7/5$ describes shock wave propagation in the absence of radiation ($q = 0$). Solution (2) for $a > 0$, i.e., $q > 0$, describes propagation of a shock wave with radiant energy absorption. A numerical solution of (1) with boundary conditions for $a < 0$, i.e., $q < 0$, describes propagation of a shock wave front with self-radiation.

Afanasenkov, A. N., I. M. Voskoboynikov, and
A. Ya. Apin. Transmission of detonation through
an air gap. IN: Detonatsiya vzryvchatykh veshchestv
i bezopasnost' vzryvnykh rabot. Moskva. Izd-vo
Nedra, 1967, 101-110.

The purpose of this work was to produce a simple criterion
for explosive sensitivity and to study the possible mechanism of transmission
of detonation through an air gap on the basis of available data. Experiments
were performed using passive charges 20 mm in diameter and 70 mm
long of hexogene of various-densities, and active charges of hexogene and
TG 50/50 of various weights and shapes. The experiments determined the
significance of explosion products and the air shock wave, and produced a
quantitative characteristic of the sensitivity of explosives to detonation
transmission through an air gap. The dependence of the distance of trans-
mission of detonation on explosive charge density was explained.

IV. SHOCK WAVES IN LIQUIDS

Kozachenko, L. S. and B. D. Khristoforov.
Parameters of a shock wave from explosion
at the bottom of a water vessel. FGiV, no. 1,
1971, 127-135.

Measurements are described of the relative pressure profile
p/p_1 (τ), duration τ, and specific impulse I of an explosive shock wave in
water vessels with three different bottom types. The measurements were
prompted by the inadequacy of known formulas, which describe a wave field
in water without allowance for significant nonlinear effects. The shock
waves were generated by the underwater detonation of a spherical explosive
charge. The shock wave parameters were measured with a minimum $\pm$ 10%
accuracy by pressure sensors. Data were recorded by PID-9 devices with
a 2 Hz - 300 kHz range. The effect of the free surface was eliminated under
the experimental conditions. Three series of experiments were carried out
in separate vessels with air-water-saturated sand (I), polystyrene (II), or
concrete bottoms (III). The three bottom types differed from each other by
the nature of their interaction with a shock wave in water. This interaction
is defined by the relationship of sound velocity a in water to the velocities C_1
of longitudinal and C_2 of transverse waves in the ground. The inequalities
$C_2 < C_1 < a$, $C_1 > a > C_2$, and $C_1 > C_2 > a$ characterize the I, II, and III bottom
types. Depth charges of 100 kg cast TNT, 1g compacted TEN, and 0.2 kg
compacted TNT were detonated in 3, 1, and 0.5 m deep basins with I, II, and III
bottoms, respectively, at relative distances H = 1-11, 1-12, and 1-4 charge
radii from the bottom. The pressure sensors were located at a depth h .
and at relative distances R = 30-120 for vessel I and 60-120 for vessel III
from the blast center, and on the periphery of a hemisphere of 0.45 m radius
for vessel II with the center at a point below the charge.

Typical oscilloscope traces of shock waves in water (Fig. 1 and
2) and the experimental $\tau(h)$ and $\tau(\alpha)$ plots (Fig. 3 and 4) are shown. The
nearly parabolic shape of the $p(\tau)$ curves (Fig. 1) suggests a nonlinear
interaction with rarefaction waves propagating from the bottom. The latter
decrease the frontal pressure, as shown by the plots of p(h). In the case
of the I type bottom, p_{max} of the reflected compression wave, which is
observed only at large angles of incidence α of the forward wave to the bottom,
attains 30% of p in the leading shock wave. A bottom wave behind and a leading
shock wave ahead of the forward wavefront were observed in the case of the
II type bottom (Fig. 2). The leading wave is generated only at an angle $\alpha \approx \alpha_o$,
which is determined by the intersection of two wavefronts. The p_{max} may
exceed by 40% the explosion pressure in an infinite liquid volume due to the
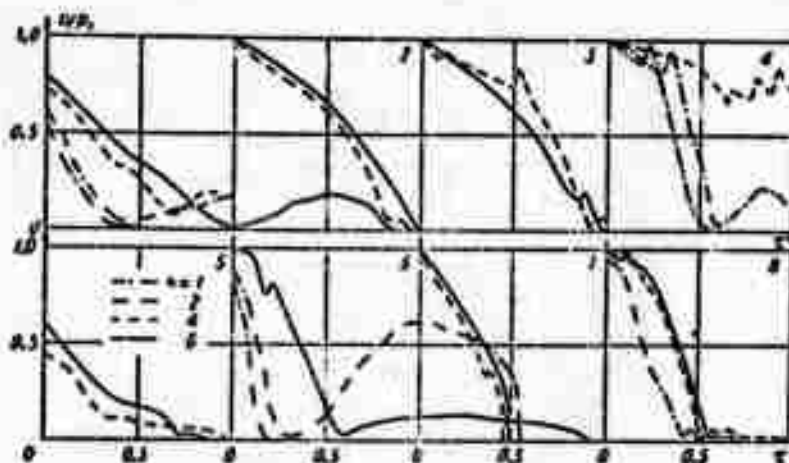
Fig. 1. Relative pressure p/p_1 versus reduced duration τ (μsec/m) of explosive shock waves in a water basin with a sand bottom.
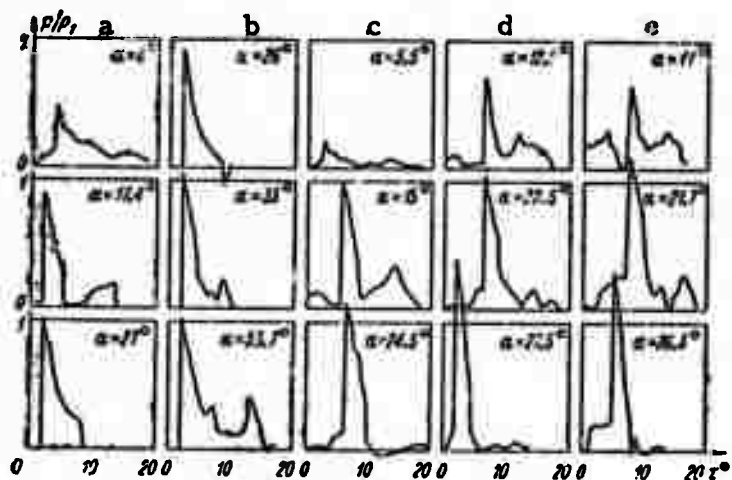

Fig. 2. Relative pressure p/p_1 versus reduced duration τ (msec/m) of explosive shock waves near the polystyrene bottom.
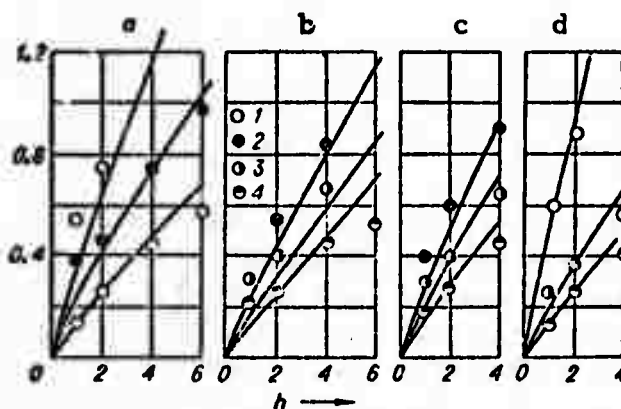

Fig. 3. Duration τ (msec/m) of shock wave versus distance h from the pickup to the sand bottom.
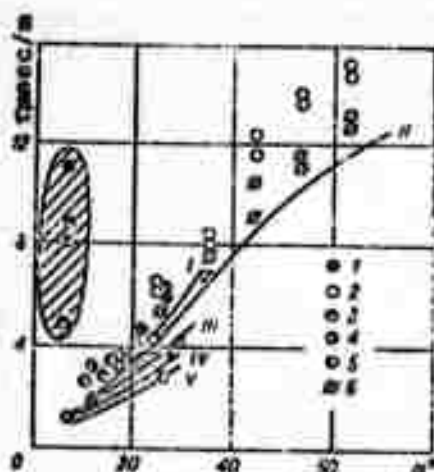
Fig. 4. Reduced duration τ (msec/m) of a shock wave versus angle α for an explosion at a polystyrene bottom.

superposition of the leading and forward wave pressures (Fig. 2, d, e). The p_{max} near $\alpha = \alpha_0 \approx 20$-$30^\circ$ increases sharply because of the interaction between the forward and leading waves, as shown on the $p(\alpha)$ plot. Interaction of the forward wave with the bottom-reflected rarefaction wave manifests itself in a decrease of τ with a decrease in α (Fig. 4). The shaded area in Fig. 4 designates the near-bottom zone, where total τ of the wave field is much longer than τ of the forward wave.

Tabulated experimental data (Table 1) show that the parameters

h	$\left(\frac{p}{p_1}\right)_e$	$\left(\frac{p}{p_1}\right)_p$	τ_e, msec/m	τ_p, msec/m	$\left(\frac{p}{p_1}\right)_e$	$\left(\frac{p}{p_1}\right)_p$
	$R=90, H=4$				$R=90, H=3$	
0	0.28	0.45	0.384	0	0.38	0.40
1	0.23	0.64	0.341	0.123	0.70	0.55
2	0.78	0.75	0.376	0.25	0.78	0.64
3	0.73	0.78	0.376	0.37	0.99	0.72
	$R=60, H=1$				$R=120, H=1$	
0	0.39	0.31	3.5	0	0.33	0.30
4	0.52	0.58	2.1	0.49	0.41	0.51
6	0.57	0.71	0.93	0.87	0.46	0.62

Table 1. Parameters p/p_1 and τ of explosive shock wave in a water basin with concrete bottom. Footnote: The indexes e and p indicate the experimental data and the data calculated from the formulas given in the text, respectively.

of the forward wave for the III type bottom are greatly influenced by the bottom-reflected rarefaction wave. The p_{max} of the forward wave decreases, when the sensor is positioned closer to the bottom, and approaches the p_{max} value calculated using an empirical formula. However, the experimental τ disagrees with the τ calculated from an empirical formula, because of the effect of a strong bottom wave.

The experimental data show that, at great distances from the blast center, the effect on shock wave parameters in water of all three bottom types is analogous to that of a free surface. The empirical formulas proposed can be used to calculate shock wave parameters. The actual τ of the shock wave measured near the bottom is usually longer than the calculated τ, because of bottom wave interference. Pressure in the lateral and leading waves is generally not over 20-30% of that in the forward wave. The maximum pressure near the intersection of the leading and forward waves is 30-40% higher than the explosion pressure measured in an infinite liquid volume. This paper is an extension of a similar work by the authors reported in Effects of Strong Explosions, no. 2, p. 111.

Podurets, M. A., G. V. Sumakov, R. F. Trunin, L. V. Popov and B. N. Moiseyev. Compression of water by strong shock waves. ZhETF, v. 62, no. 2, 1972, 710-712.

Measurement of shock compressibility of water by absolute methods is limited to a maximum pressure of 1~2 Mbar. For higher pressures, compressibility can be found only by relative methods, based on a reliable interpolation of the impact adiabatic curve of a standard analog substance, which in case of water can be aluminum. In this article the authors use the cited method to investigate the relative compressibility of water at pressures ~ 14 Mbar. The measurements were obtained by successive recording of a shock wave propagating through an aluminum block of thickness $\Delta = 160$ mm and a water layer of thickness $\Delta = 80$ mm; wave velocity (D) was determined with an error $< 1\%$. Parameters of compressibility, according to this known wave velocity, were determined by P-U diagrams (pressure - body velocity of the substance behind shock wave front). Damping of the shock wave at the interface between aluminum and water surfaces is taken into account by a small correction in the calculations. Initial parameters in aluminum are found to be $D_{Al} = 36.40$ km/sec; $U_{Al} = 25.55$ km/sec; $P_{Al} = 25.20$ Mbar, and for water they are $D = 43.95$ km/sec, $U = 32.42$ km/sec, $P = 14.25$ Mbar, and $\rho = 2.815$ g/cm^3. Errors in determining the water density are connected with the experimental inaccuracy in measuring the wave velocity in both media, and also with the uncertainty in the standard adiabatic curve for aluminum; they amount to about $\Delta e/e \approx 0.03$. Results are plotted in Fig. 1. The figure includes a curve calculated according to the quantum-statistical Thomas-Fermi model. A comparison of calculated and extrapolated experimental dynamic adiabatic curves
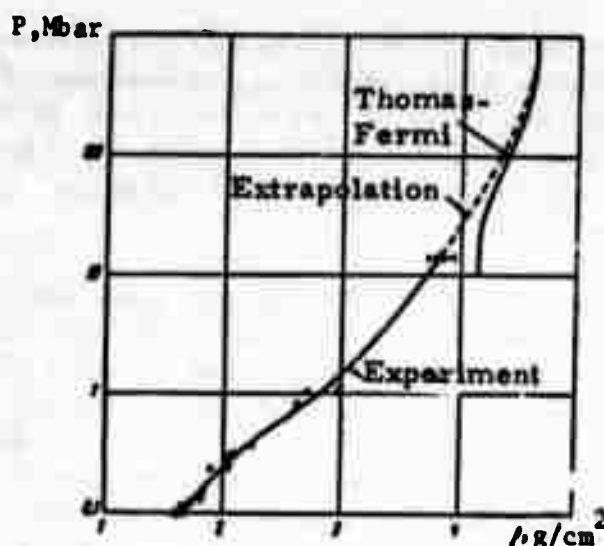
Fig. 1. Shock adiabats of water.
▲ - authors' results
○} - experimental adiabats, other authors.

of water shows the applicability of the Thomas-Fermi model for determining the parameters of compressibility for relatively light substances such as water in the region of very high pressures, $P \geq 400$ Mbar.

Ocheretin, V. N. Study of shock wave formation from exploding wires in water. EOM, no. 5, 1971, 39-41.

A description is given of an experiment on the formation of shock waves in water from an exploding wire. The experimental sketch is given in Fig. 1. Tests were conducted with steel and copper wires of 0.15 mm dia and 90 mm length, each with an initial voltage of 50 kv and a discharge capacity of $1 \mu f$. Photographs were taken at the rate of 600,000 frames per second; two photographs are given illustrating steel and copper wire explosions. It was noted that the channel formed from the explosion of a steel wire had a uniform structure, while that formed by copper wire was nonuniform. Energy levels in the channels were measured at 150 kj/cm^3 and 115 kj/cm^3 for steel and copper wire respectively. From the test results, the author recommends use of steel wires, rather than copper or brass, for its superior hydrodynamic parameters.
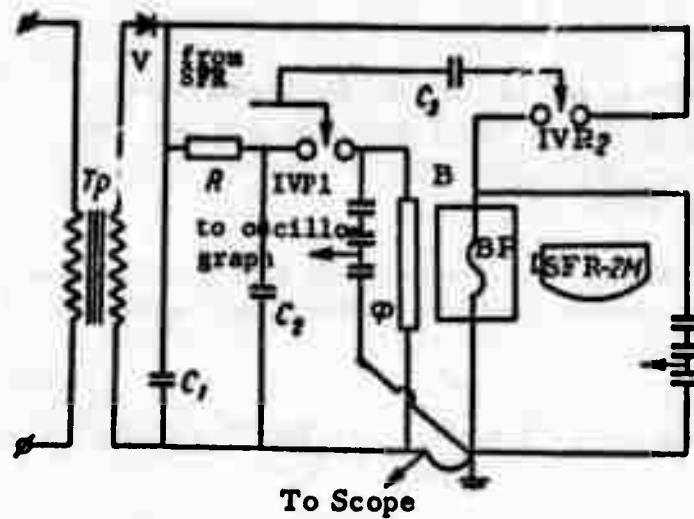
To Scope

Fig. 1. Experimental diagram. TR -
high voltage step-up transformer; V -
rectifier; IVP1, IVP2 - spark gaps;
B - test vessel; φ - aluminum foil;
BP - exploding wire.

". SHOCK WAVES IN SOLIDS

Limarev, A. Ye. and A. D. Chernyshov.
__Propagation of shock waves in a reinforced__
__elasto-plastic medium.__ PMM, no. 6, 1971,
1083-1088.

Propagation and structure of shock waves in a translationally
-reinforced elasto-plastic medium is described by the closed set of discontinuity equations

$$[\sigma_{ij}{}^{*}] - 2\mu_1 [e_{ij}{}^{*}] = 2[\varphi] \{2\mu_1\mu_2 e^{*\frac{+}{ij}} - 2\mu_0 s^{*\frac{+}{ij}} - \mu_1\mu_3 [e_{ij}{}^{*}] + \mu_0 [\sigma_{ij}{}^{*}]\} + \ldots \qquad (1)$$

$$[\sigma_{kk}] = (3\lambda_1 + 2\mu_1) [e_{kk}] \qquad (2)$$

$$\left[\sigma_{ij}{}^{*} - \frac{\mu_1\mu_2}{\mu_0} e_{ij}{}^{*}\right]\left\{2\left(\sigma_{ij}{}^{*} - \frac{\mu_1\mu_2}{\mu_0} e_{ij}{}^{*}\right)^{+} - \left[s_{ij}{}^{*} - \frac{\mu_1\mu_2}{\mu_0} e_{ij}{}^{*}\right]\right\} = 0 \qquad (3)$$

and

$$[s_{ij}] v_j = -\rho^{+}G[v_i], \quad [u_{i,j}] = \omega_i v_j, \quad [v_i] = -G\omega_i \qquad (4)$$

where σ_{ij}, σ_{kk} are stress components, e_{ij} are strain components, λ_1, μ_0, μ_1, μ_2 are elastic coefficients, v_j is normal to discontinuity surface, G is the propagation velocity of a nonremovable discontinuity surface in a continuous medium, U_i, V_i are the displacement and velocity of a particle, and the asterisk denotes a tensor deviator component. Equations 1-4 were derived assuming a linear dependence between two discontinuous functions within the shock wave transition layer. This linear approximation made possible a common solution to the problems of propagation and structure of shock waves in a plastic noncompressible material.

Using (1) and (4), an expression is derived for the characteristic of irreversible plastic deformation of a continuous medium

$$2[\varphi] = F_1\omega_n (\mu_0\omega_n F_2 - \mu_1 s_{nn}^{p+})^{-1}{}_s^{!}$$

$$[F_1 = \rho^{+}G^2 - \lambda_1 - 2\mu_1, \quad F_2 = \rho^{+}G^2 - \lambda_1 - {}^2/{}_3\mu_1 (1 + \mu_2/\mu_0)$$

where S_{nn}^{p+} is the stress component of a plastic element p of the rheological model of the material, the index n and the sign + indicate direction of the

normal v_i and the value ρ ahead of the shock wavefront, respectively. The velocity ρ^+G^2 of discontinuity surface propagation is determined by the roots of the equation of the 4th degree in ρ^+G^2, which was derived from the equations 1-5. The root $\rho^+G^2 = \mu_1$ of the cited equation corresponds to a transverse neutral wave without discontinuity of plastic deformation and satisfies the condition $\left[\varphi \right] = 0$. This particular case is illustrated by an example of a rectangular elasto-plastic plate subjected to either a tensile or a shear stress. Two other roots of the 4th degree equation indicated the possibility of generating two plastic shock waves in a three-dimensional re-inforced elasto-plastic medium. One of the plastic waves propagates in a medium under spherically symmetric stress, the other in a medium where $S_3^{p*+} = 0$.

Godunov, S. K., A. A. Deribas, I. D. Zakharenko, and V. I. Mali. Investigation of viscosity of metals during high velocity shock. FGlV, no. 1, 1971, 135-141.

This article describes a study of metal viscosity during shock from explosive welding. An experiment is described in which steel plates were welded as shown in Fig. 1. On detonation of explosive (5), the upper plate (3) is driven onto the lower plate (1), as a result of which the two plates are welded as shown in Fig. 1b. The welded specimen was then cut along the direction of
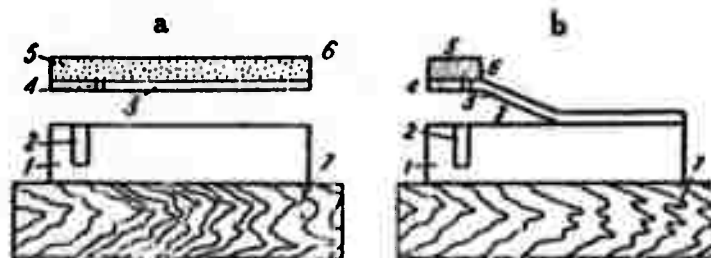

Fig. 1. Explosive weld.
1, 3 - steel plates; 2 - slot; 4 - hole
(0.3~0.5 mm); 5 - explosive; 6 - detonator;
7 - wooden base.

movement of the contact point and the cross-section was microphotographed (Fig. 2). Horizontal displacement z with relation to the distance y from the

interface was measured on the photograph. At $y > \delta_1$ (δ_1 - thickness of upper plate, δ_2 - thickness of lower plate), the relationship between z and y follows a parabolic curve, $z = a(y - \delta_2)^2$; while at $y < \delta_1$, $z = be^{-ky}$ - an exponential curve (a, b = constants). Displacement of impact points of the plates with relation to metal viscosity was investigated and was found to be inversely proportional to viscosity. Mathematical expressions are derived for determining stored impulses and the diffusion of horizontal velocities in both upper and lower plates. Using experimental data and derived formulas, viscosity coefficients were determined for Al, Cu and steel (Table 1). Viscosity coefficients for Al, Cu and steel are seen to have an increasing order of $(0.3 \sim 0.8)10^5 p$, $(2 \sim 2.7)10^5 p$ and $(4 \sim 5)10^5 p$ respectively.

Fig. 2. Microphotograph of weld section.
1 - lower plate; 2 - compressed plate;
3 - upper plate; 4 - compressed wire.
Arrow indicates the direction of detonation.

The authors compare these values with those of Popov (Inzhenernyy sbornik, 1941, 1, 1) and Il'yushin (Inzhenernyy sbornik, 1941, 1, 1), and the value of viscosity coefficient for steel is found to be the same in both cases. Similarly, the obtained value for Al is found to be in good agreement with the results of Sakharov, Zaydel', et al (DAN SSSR, 1964, 159) and Mineyev and Savinov (ZhETF, 1967, 57, 3). However, according to the results of Il'yushin (Uchenyy zap. MGU, Mekh, 1940, 39, 11 and Inzhenernyy sbornik, 1941, 1, 1),

aluminum and steel have approximately the same coefficient of viscosity (about 10^5p), which lies far below the results of Table 1. Similarly, works of Sakharov, Zaydel', etc, as well as Mineyev and Savinov, disagree with the present results in the fact that in their results Al, Cu and steel all have the same viscosity value. The authors discuss these discrepancies, and express doubts as to the accuracy of the cited other experiments.

Materials	l_1, cм	l_2, cм	$v \cdot 10^{-5}$, cм/sec	τ	$\mu \cdot 10^{-5}$ poise	
					$\gamma=0.4$	$\gamma=0.8$
Al (Д 16)	0.4	2.0	2.5	10°30′	0.31	0.32
	0.4	3.0	3.1	14°	0.81	0.86
Cu (M 3)	0.4	1.4	1.7	21°	2.1	2.7
	0.4	2.4	4.2	14°20′	2.5	2.0
Steel(Ст. 3)	0.45	2.8	3.1	15°20′	3.9	4.1
	0.4	3.0	4.0	14°20′	4.8	4.8

Table. 1. Shock viscosity results.

Zubarev, V. N. Shock wave compression of piezoelectric ceramics. ZhPMTF, no. 2, 1971, 106-110.

Dynamic compressibility and piezoelectric characteristics of type TsTS 53/47 lead zirconate titanate ceramic samples were measured at pressures in the 100-500 kbar range in front of a shock wave. Also, nonreversible changes were observed in the samples after their short-time compression at 350 and 500 kbar. Shock waves from detonation of an explosive charge were transmitted to the sample through a metallic screen. The measured wave velocities U in the sample and the calculated mass velocities u, pressures p, and temperatures T were tabulated. An experimental plot of p versus specific volume V shows, in contrast to earlier American data, the absence of a two-wave shock structure in the 100-350 kbar range; the linearity of the U - u dependence confirmed this finding. The measurement of current during shock wave transmission indicated only small variations in polarization at a load ≥ 1 ohm, so that inductance D_1 can be approximately described by $D_1 = D_0 + \epsilon_0 E$. It follows that dielectric constant ϵ and electric conductivity λ in a compressed sample can be calculated from the equation of R. M. Zaydel' [ZhETF, v. 54, no. 4, 1968] using the experimental extreme values of current. Calculations revealed that λ is relatively high ($\sim 4.5 \times 10^{-3}$ ohm^{-1} x cm^{-1}) at p = 105 kbar, and increases by a factor of about 20 at

467 kbar. The density of samples following shock wave compression at 350 and 500 kbar increased from 7.35 to 7.7 - 7.8 g/cm^3, and the samples were completely depolarized. Analysis of the data led to the conclusion that conversion to the paraelectric phase is possible at shock wave pressures in the 300 - 400 kbar range. An analogous experiment by Zubarev et al on shock compression of plastics was reported in Explosion Effects Report no. 2, p. 4.

VI. FLOW PAST BODIES

Balakin, V. B. and V. V. Bulanov. A numerical solution of the problem of interaction of a sho: wave with a cylindrical body in supersonic flow. IFZh, v. 32, no. 6, 1971, 1033-1039.

A two-dimensional finite difference scheme of the second order accuracy is introduced to compute the process of collision of a nonstationary shock wave with a stationary flow around the nose-end of a cylinder moving at a supersonic speed. The initial set of equations of two-dimensional flow in divergent form is presented in vector notation

$$\frac{\partial f}{\partial t} + \frac{\partial}{\partial x} F(f) + \frac{\partial}{\partial y} G(f) + \frac{v}{y} H(f) = 0 \tag{1}$$

and allowance is made for through computation of shock waves. Eq. (1) is then approximated in two steps by a finite difference equation which contains artificial viscosity terms in the x and y directions measured along and from the flow axis, respectively. The necessary and sufficient stability criteria of the finite difference scheme

$$\left(\frac{\Delta t}{\Delta x} A\right)^2 \leqslant \frac{1}{2} E, \quad \left(\frac{\Delta t}{\Delta y} B\right)^2 \leqslant \frac{1}{2} E \tag{2}$$

were established by a Fourier method. A = dF/df and B = dG/df in (2) are Jacobians of the F and G vectors in a random point of the flow, Δ x and Δ y are the difference grid pitches along x and y, Δ t is the time pitch, and E is the matrix unit. By use of a through computation method, a commong numerical solution is outlined for two corollary problems: the initial supersonic streamline flow around the body, and the oncoming shock wave with establishment of a new regime of supersonic streamline flow. The initial flow parameters are those of the first shock wave. The parameters of the second shock wave are calculated by means of Hugoniot formulas. Numerical solutions of the problem are illustrated graphically.

Poluboyarinov, A. K. Propagation of a
shock front reflected by a blunt body.
MZhiG, no. 2, 1971, 70-77.

Shock wave front interaction with a blunt sphere or cylinder is
analyzed on the assumption that the front plane is normal to the symmetry
axis or plane of the body and, in the case of the cylinder, is parallel to the
body generatrix. An exact differential equation is derived to describe
nonstationary separation of the symmetry center of the shock reflected by a
static body. The equation describes dimensionless axial shock separation ϵ
as a function of the independent variable M of the reflected front. The equation
also contains two additional unknown quantities: the derivative $(\partial v/\partial x)_1$ of
gas velocity immediately behind the shock, and the radius r of the reflected
shock front curvature along the symmetry axis. An exact formula was
derived for initial $(\partial v/\partial x)_{1*}$ as a function of r_* and M_*. Approximate
formulas define r_* and $(dr/d\tau)_*$ in the initial separation phase of the front
from the body. A fairly simple approximate method is introduced to
determine nonstationary ϵ for a sphere, on the basis of the derived formulas
and the precise equation of ϵ. The method consists of integrating the
equation $d\epsilon/dM = \varphi$, where φ is a function of r and $(\partial v/\partial x)_1$. A numerical
example shows that the method correctly describes the initial separation
phase, and also its final phase if a correction to the φ function is introduced.

Yeliseyev, Yu. B. and A. Ya. Cherkez. The
effect of an increase in stagnation temperature
in a streamline gas flow past a deep cavity.
MZhiG, no. 3, 1971, 8-18.

An earlier observed anomalous increase in temperature of
the separated gas flow within a cavity above the stagnation value T_0 is
discussed, on the basis of a theoretical model of compression and decom-
pression waves in a cylindrical tube. Piston oscillatory movements at the
open end of the tube model simulate conditions at the streamline flow-separated
gas interface. Characteristics of the nonstationary self-oscillating shock
wave process at the interface are formulated and a numerical example is
given. A preliminary conclusion was drawn that the observed phenomenon
is reproducible with models of different dimensions but is influenced by
increased boundary layer thickness. Aerodynamic experiments with different
models at M < 1 and M = 1.6 and 2.0 are described. In agreement with
theoretical calculations, the stationary air temperature at the base of a
model increased by a minimum of $100°K$ above T_0. The experimental data
confirmed the hypothesis that the shock wave thermal effect and heat release
follows energy dissipation in shock waves. The intensity of the observed

effect depends greatly on the shape of the leading edge and the angle formed by the model exit section plane with the axis. The experiments suggest the possibility of reproducing the effects in the surface cavity of an object flying in the atmosphere. Methods for minimizing the undesirable thermal effect are given.

Bezhanov, K. A. Diffraction of a shock wave on a wedge moving at supersonic velocity. Prikladnaya matematika i mekhanika, no. 4, 1969, 631-637.

A theoretical study is made of the diffraction of an arbitrarily strong shock wave on the surface of a wedge, moving with supersonic velocity. Using the notations of Fig. 1, the author assumes that the incident angle δ of
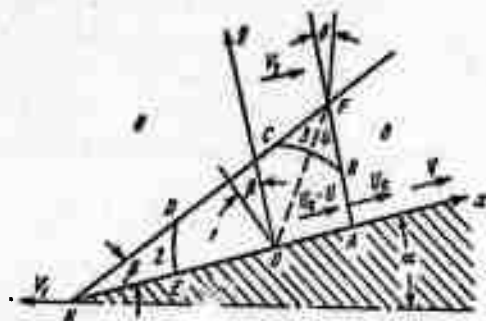

Fig. 1. Flow model.

the shock wave is approximately the same as the wedge angle α. In this notation U_0 defines absolute shock wave velocity, while U is its velocity relative to adjacent flow. With the use of some simplifying assumptions the analysis is made with a linearized equation for planar gas flow, using dimensionless parameters. The work is an extension of some cited earlier treatments of a similar problem in which diffraction of the shock wave was assumed not to take place.

Borovoy, V. Ya. and M. V. Ryzhkova. Heat transfer on a semi-conic surface at high hypersonic velocities. MZhiG, no. 4, 1969, 137-142.

Formation of narrow bands of intensive heat transfer on the flat surface near the edges of a streamlined spherically-blunted semi-cone (Fig. 1) was studied experimentally at a Reynolds number Re in the 1.5×10^5 - 2.4×10^6 range. At a sufficiently high Re, the boundary layer separates
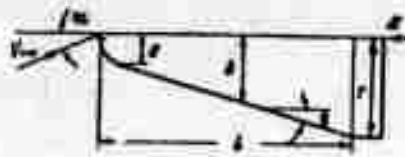
Fig. 1. Spherically blunted semi-cone.

from the flat surface and two separate vortex formations appear near the edges as boundary lines along the surface. Most of the heating occurs along the boundary lines where heat transfer coefficient h^o may be several times higher than h^o on the remaining part of the flat surface. The experiments show that Re is the most important factor in formation of the boundary lines of intensive heat transfer. At $Re = 2.5 \times 10^4 - 10 \times 10^4$, h^o_{max} increases nearly proportionally to Re, while at $Re > 10 \times 10^4$ the rate of h^o_{max} increase is somewhat slower. The strong effect of Re confirmed the assumption that the laminar flow changes to turbulent at the boundary of the separation zone. Boundary layer separation occurs because of an over-flow of gas from the conic to the flat surface. This was confirmed by an experiment with a barrier. Experiments with a reduced thickness boundary layer and increased conic surface roughness did not contradict the proposed flow pattern.

Myshenkov, V. I. Subsonic and transonic viscous gas flow in the wake of a two-dimensional body. MZhiG, no. 2, 1970, 73-79.

Viscous gas flow in the wake of a finite thickness plate is analyzed at subsonic and transonic velocities, Prandtl number = 0.71, and Reynolds numbers R in the 1-1,000 range. The problem is formulated by Navier-Stokes equations for given flow parameters at infinity and at a finite distance from the bottom of the plate. Equations of state and motion are solved by approximation of a finite-difference scheme in two steps. A numerical solution which satisfies the condition of a steady flow is presented graphically for different R and M values. The solution shows that at $R \leq 1.7$ gas flows without separation from the bottom, and at $R > 1.7$ a region of reverse flow with separation forms at the stagnation point. The reverse flow region expands with increase in R and the separation point shifts upwards in the direction of the angular point of the plate. A deformation of the reverse flow region with a decrease in relative velocity of reverse current is observed at R = 100 at increased M (from 0.288 to 1.15). The flow patterns are in agreement with earlier theoretical and experimental data. Pressure variation patterns at the bottom of the plate are also shown in the flow plane and the plane normal to flow.

Stulov, V. P., and L. I. Turchak. Non-
equilibrium chemical reactions in a shock
layer in a streamline flow of a carbon dioxide
-nitrogen-argon mixture around a sphere.
MZhiG, no. 5, 1969, 147-150.

A theoretical evaluation of hypersonic (M = 16-20) flow of
CO_2-N_2-Ar mixtures around a sphere was made using a known physico-chemical
model of a shock-heated gas mixture. The model presumes the existence
of nine components in the shock layer, with allowance for five molecular
dissociation and five atom exchange reactions which are tabulated. Dissociation
rate constants were calculated for collisions with particles of different
catalytic activity. The presence of O_2 was disregarded in the establishment of
the model, and molecular vibrations at $T \geq 4000^\circ K$ were considered to be at
equilibrium. It was shown that the flow changes significantly with a change
in relative concentrations γ_∞ (CO_2) and γ_∞ (N_2) in the shock layer. Shock
wave separation increases by ~50% when γ_∞ (CO_2) is decreased from 0.95
to 0.05, and thermal energy absorbed by the gas simultaneously increases
because of a decrease in T and an increase in the fraction of atomic components.
The effect of Ar addition is analogous to that of N_2. Most of the heat is
absorbed by CO_2 dissociation because of its higher rate.

Shifrin, E. G. Formation of a "hanging"
compression shock in the streamline flow
past a profile with a broken generator. PMM,
no. 6, 1970, 1159-1167.

Uniform supersonic streamline flow past a profile with a
convex salient point is analyzed in the case of an oncoming stream with a
low supersonic velocity, when entropy changes in the shock wave can be
disregarded. The region behind the shock wave is projected on the hodograph
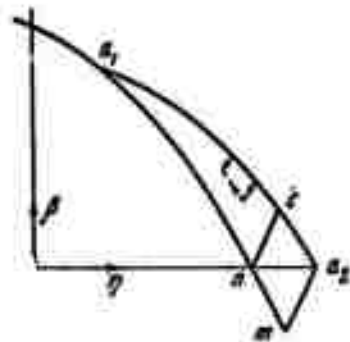

Fig. 1. Projection of the flow behind
shock wave on hodograph plane η - β .

plane $\eta - \beta$ (Fig. 1) where $\eta = (k + 1)^{1/3}(\lambda - 1)$, β is the inclination of the velocity vector to the symmetry axis, λ is the velocity factor, and k is the adiabatic exponent. A streamline flow with attached shock wave past a profile formed by straight line intercepts is considered in a first approximation. The equations of the shock polar β and intersecting characteristics, e.g., $a_1 a_2$, are given in a transonic approximation. Proof is offered that a single "hanging" shock is necessarily generated behind the shock wave. The "hanging" shock propagates downstream from its starting or end point which is located at an infinite distance from the profile. The shock at $\beta_0 \leq 0$ is convex in relation to the flow behind it. In addition to the tail shock, there is an internal shock, at $\beta_0 < 0$, which intersects the tail shock and forms a lambda-shaped shock.

Antonets, A. V. Computation of three dimensional supersonic flow past blunt bodies with generator breaks and allowance for equilibrium and frozen states of the gas in the shock layer. MZhiG, no. 2, 1970, 178-181.

An algorithm is developed for computation of the steady supersonic flow of an inviscid gas past a blunt body with multiple breaks of a generator. The algorithm is based on the principle of separation (behind each of an arbitrary number of breaks) of the regions of smooth solutions between the body and the characteristic shock wave surfaces, at a positive (expansion) or negative (compression) break. Finite-difference equations in the nodal points of a net are substituted for differential equations in the regions of smooth solution. The unknown velocity components, pressure p, and enthalpy i are determined from the equations by the method of successive calculations. The algorithm accounts for the effect of nonequilibrium physicochemical reactions by computing the flow for either the entire shock layer in a nonequilibrium (frozen) state or for only a partially frozen layer in the area adjacent to the body surface, the other part being occupied by a gas at equilibrium. The effect of the gas equation of state in the shock layer is illustrated by p(x) plots for the flow past a spherically blunted cone with an apex half angle $\theta \leq 10°$. The plots show that at $\theta = 10°$ p in some points on the surface in a flow at equilibrium can be twice that in the frozen flow. The computation method may be useful in evaluating actual flight effects at altitudes above 60 km and at velocities of 6,500 m/sec or greater.

Antonets, A. V., A. V. Krasil'nikov, and
V. I. Lagutin. Experimental determination of
the position of pressure center in hypersonic
gas flow around a blunted cone at different
angles of attack. MZhiG, no. 2, 1971, 142-143.

Following from the previous paper, the relationship between
the position of a pressure center C_d and an angle of attack α was determined
in a hypersonic wind tunnel at $M_\infty = 6$ and 15 and Reynolds number $Re \approx 10^6$
using a spherically blunted test cone. The cone had a sphere radius R,
relative conic length x/R = 5, and apex half-angle $\theta = 11^\circ$. The highly accurate
method of free aerodynamic balance was applied while varying the distance
x_0 of the rotational axis from the cone nose. The C_d value for a balanced α
coincides with x_0. Plotted experimental C_d data (Fig. 1) agree within a 2%
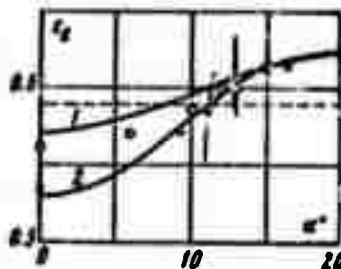

Fig. 1. Pressure center C_d versus angle
of attack: curves 1 and 2 - calculated for
$M_\infty = 6$ and 15, respectively; small circles
- experimental data for $M_\infty = 6$; points -
experimental data for $M_\infty = 15$.

maximum discrepancy with theoretical data calculated by the method of
Antonets cited in the previous paper [MZhiG, no. 2, 1970, 178], but
disagree with the $C_d (\alpha)$ data calculated by the Newton formula (dotted line).
Results suggest that physical phenomena on the leeward side of a cone at
$\alpha \geq \theta$ do not significantly affect aerodynamic characteristics.

Voronkin, V. G. Nonequilibrium viscous
flow of a multicomponent gas near the stagnation
point of a blunt body. MZhiG, no. 2, 1971, 144-147.

A theoretical study is made of the effect of shock layer variable
parameters on heat transfer, in the case of nonequilibrium-dissociated
air at a barrier of finite catalytic activity near the stagnation point of a
spherically blunted body. Heat transfer in the nonequilibrium outer flow is
compared to that in an equilibrium-dissociated gas flow. Numerical

calculation of the nonequilibrium flow was based on the concept of a compressed viscous shock layer. Only free-stream Reynolds numbers R above 1,500 were considered. Under these assumptions, the calculation was reduced to a solution of the boundary layer equations with boundary conditions corresponding to those immediately behind the leading shock wave. Temperature profiles, concentrations of oxygen and nitrogen atoms in the shock layer, and the relative heat flux Q_w were calculated at a 60 km height, 7.4 km/sec free-stream velocity, 700°K wall temperature and 1-100 cm radius of curvature R. It was shown that Q_w in the nonequilibrium shock layer at small R can be significantly increased (by a factor of 3) in relation to the theoretical Q_w in an asymptotically thin nonequilibrium boundary layer with equilibrium parameters at its outer boundary. At increased R the vorticity effect decreases and the effects of nonequilibrium chemical reactions become predominant.

Lunev, V. V., and N. Ye. Khramov. Flow past a blunt body near the stagnation point in a divergent hypersonic stream. MZhiG, no. 3, 1970, 102-105.

The inhomogeneous hypersonic outer stream near the stagnation point past a blunt smooth body is analyzed at a small ratio k of densities ahead of and behind a straight shock wave. Thickness δ of the shock layer at the forward stagnation point is formulated by

$$\frac{\delta}{kR_*} = \frac{1}{2}\ln\frac{2}{k}, \quad \nu = 0$$

$$\frac{\delta}{kR_*} = \frac{1}{1+\sqrt{2k}} \quad (\nu = 1) \tag{1}$$

where R_* is the effective curvature radius of the body and $\nu = 0$ and $\nu = 1$ refer to two-dimensional and axisymmetric flows. The formulas in (1) were derived from equations of motion assuming gas density to be constant. It follows from (1) that δ, and hence the profile of the shock layer, depend on k and R_* only. This dependence is illustrated by computed δ(k) plots for an axisymmetric, strongly underexpanded conic jet around a sphere. The initial flow parameters are tabulated. The data all lie on the same curve which coincides with the theoretical curve calculated for $\nu = 1$ and R_*/R boundary values. Plots of pressure distribution p/p_0' along a barrier versus x/R ratio diverge significantly for different jets, but the same plots of p/p_0' versus x/R_* form a relatively narrow band which is close to the plot for a sphere in a homogeneous stream and the Newtonian plot. The effect of stream divergence is thus accounted for by introduction of R_*. The effects of nonuniform density and velocity of the oncoming stream are taken into account in an analogous manner.

The flow generated at the upper surface of a moving wedge by
an oncoming plane shock wave was analyzed. Conditions are formulated for
the flow according to the pattern shown in Fig. 1. It was assumed that intensity
of the oncoming shock wave CE was equal to that of the attached compression
shock OA, CE is normal to OB, and the interacting shocks CD and DA are
weak and reflected at a $\psi/2$ angle by a rigid wall with resulting refraction,
but without formation of a third shock wave. It is shown that, under these
assumptions, the flow past the wedge upper surface OB can be calculated using
linearization theory, if a point, defined by the Mach number M of the oncoming
flow and the angle δ of the wedge, lies within certain boundaries in the M-δ
plane. All the conditions were verified within an area bound by the curves
$f_1 (M, \delta) = 0$, $f_2 (M, \delta)$, $f_3 (M, \delta)$, and the abscissa. If the point defined
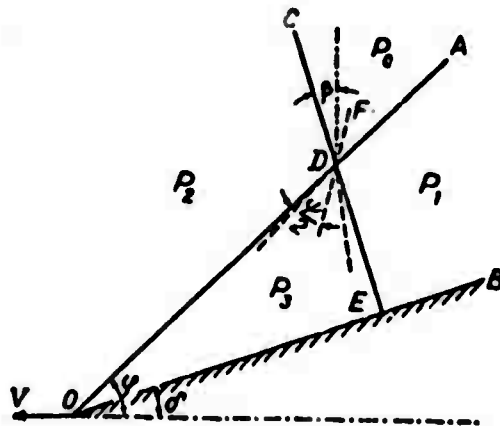

Fig. 1. Flow diagram on the upper
surface of a wedge.

by the wedge parameters M and δ lies within this area, the flow will be
uniform. Pressure p_3 within the area is then given by

$$\frac{p_3}{p_0} = 1 + \frac{2\gamma M^2}{\sqrt{M^2-1}} \delta \qquad (1)$$

where p_0 is the pressure generated by interacting shocks and γ is the
adiabatic exponent.

Mamadaliyev, N. A., and Kh. A. Rakhmatufin.
Streamline fluid-solid, two-phase flow past
a slender profile. IN: Volny v neuprugikh
sredakh (Waves in nonelastic media). Kishinev,
AN Mold SSR, 1970, 146-152.

A mathematical model of a fluid-solid supersonic flow past a
slender profile, e.g., a wedge, is introduced for use in calculations of jet
parameters from supersonic nozzles, flight mechanics in a gas-dust medium,
etc. The model makes allowance for post-shock reflection of particles from
the profile surface. For a specific volume <1, the effects of particles on the
gas flow and friction between particles in the region of a three-velocity
flow can be disregarded. Solution of linearized equations of motion for
particles impinging on and reflected from a wedge with a given apex angle
β_0 thus leads to the conclusion that the boundary between the three-velocity
and the two-velocity flows is a straight line with slope $\beta = 2\beta_0$. The
boundary condition at $y = 0$ is also a straight line, and formulates the law
of mirror reflection. For the case of a two-phase medium with a significant
particle concentration, and disregarding the effect of the reflected stream,
a solution to the inverse problem is presented in the form of an equation of
the profile surface for a given flow separation boundary with a constant
inclination β. In contrast to the first analyzed case, the profile surface is
weakly concave in relation to the stream, and the three-velocity region II
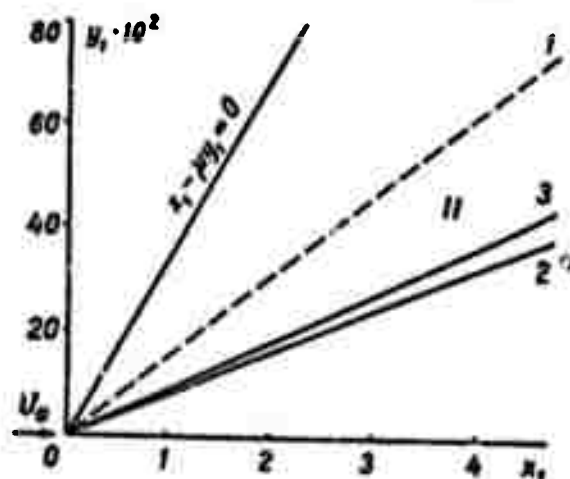narrows with the increase in X_1, as shown in Fig. 1.

Fig. 1. 1 - separation line, profile surface;
2 - at a small and, 3 - at a significant
particle concentration.

Lunev, V. V. Nonviscous flow near the
critical point of a blunt body having a variable
density along its axis. MZhiG, no. 6, 1971,
56-61.

The flow in a thin compressed layer around a smooth blunt
body is described, in the framework of hypersonic theory. A set of
conservation equations is derived using an x, y curvilinear coordinate system
with the stagnation point as origin. A localized closed solution near the
stagnation point is possible when the shape of the shock wave approaches
that of the body and the ratio k of densities ahead and behind the shock
wave tends towards zero. A solution in the vicinity of the axis is sought
in the form of an expansion in xK powers:

$$v = -v_\bullet(y) + \dots, \quad u = K x u_1(y) + \dots, \quad r = x + \dots$$
$$p = p_\bullet(y) - K^2 x^2 \beta(y) + \dots, \quad k\rho = \rho_\bullet(y) + \dots \tag{1}$$

where $K = R^{-1}$ is the body curvature, uV and vV are velocity components
along x and y axes, of the incident flow, r is the distance from the symmetry
axis, and ρ is density. By substitution of variables, conservation equations
are derived, which are similar to adiabatic flow equations for a perfect gas
with nearly constant ρ. Derivation of the Busemann formula from (1)
indicated that universality of pressure distribution can be extended to the
entire front surface of a smooth body. The Busemann formula also led to
the conclusion that the asymptotic pressure distribution along the body is
independent of flow physics. Analysis of boundary conditions revealed two
possible boundary flow patterns. According to one pattern, ρ distribution in
the vicinity of the wall satisfies the condition

$$\varphi \lesssim \text{const}\, \zeta^{2/(1+\eta)} \lesssim k \tag{2}$$

i.e., the solution in similar variables ζ, t, including t δ, depends only on
the body values of ρ distribution and the axial pressure gradient (at $\zeta = 0$),
and is the same as the solution in the case of a constant $\rho = k_0^{-1}$ along the
thickness δ of a shock layer. The solution of (2) for an axisymmetrical flow
is shown to be weakly dependent on k_0, except for a narrow near-wall region
of the order $t \sim k_0^{\frac{1}{2}}$. The solid lines in Fig. 1 are plotted for the condition
$k_0 = 0.1$. The t$\delta = \eta_\delta / k = 0.80$ value calculated from the plots in
Fig. 2 in effect coincides with the $\delta / kR \simeq 0.78$ value, which was obtained
earlier for a streamline flow of dissociated air at an equilibrium within
k = 0.05 - 0.20 range. But the true thickness δ / kR calculated for curves
1-5 depends significantly on ρ distribution. The solution for a two-dimensional
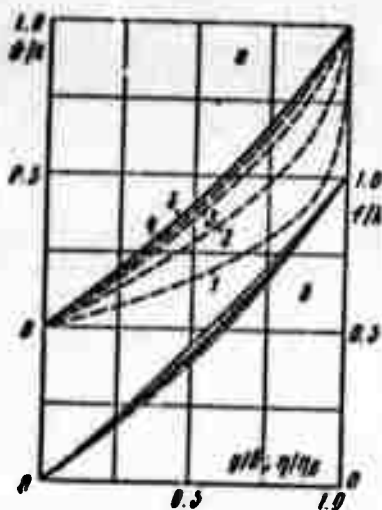
Fig. 1. Axial velocity profiles versus
initial coordinate y/δ ; the numbers 1-5
at the curves correspond to those in Fig. 2.
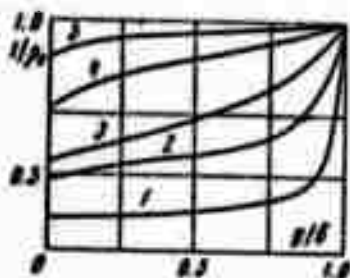
Fig. 2. Density profiles versus initial
coordinate y/δ for an axisymmetric flow.

flow $(v = 0)$ is seen to be always dependent on k_o; but the dependence on
$k_o = 0.05 - 0.2$ is weak as shown in Fig. 3, where the plots 1-4 correspond
to $k_o = 0.2$, 0.05, 0.01, and 0.001. A certain degree of universality of the
$\zeta(\eta/\eta_\delta)$ function is consequently also to be expected in the case of two
-dimensional flow.

Fig. 3. Axial velocity profiles versus
similar coordinates ζ, t. for a two-dimensional
flow.

According to the second flow pattern, ρ distribution near the wall exhibits a singularity. A significant variation occurs in t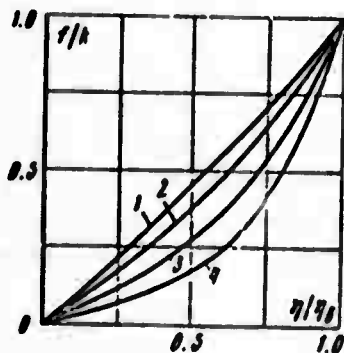he ρ profile which is bound to affect the flow, particularly in the near-wall layer. Even in this case, however, the $\int(\eta/\eta_\delta)$ profile is expected to remain universal, because of the weak dependence of the solution on the parameter k_o, i.e., the gas ρ near the wall.

It is concluded that in all except the near-wall sublayer case, the solution should be the same as for a constant ρ equal to the ρ value behind the shock wave. Calculation of the structure of an inviscid shock layer can thus be simplified, given the universality of the axial flow profile in $\int, \eta$ variables.

Neyland, V. Ya. Upstream propagation of perturbations from interaction of a hypersonic flow with a boundary layer. MZhiG, no. 4, 1970, 40-49.

Hypersonic viscous gas flow past a slender body is analyzed for weak, moderate and strong free interactions. In the case of a weak hypersonic interaction, perturbations generated in the vicinity of a singular point, (e. g., bottom cut or angular point), are seen to propagate upstream a short distance only. Locally nonviscous flow regions may also form with high pressure gradients. Boundary layer separation into sub-regions of different sizes disappears in the presence of a moderate or strong hypersonic interaction. The perturbations in this case propagate up to the leading edge of the body in the process of free interaction along the entire boundary layer. Proof was obtained that localized flow regions of very high pressure gradients are not generated at the interaction parameters $X \geq 1$. The possibility exists, however, of a separation zone formation on the order of magnitude of one body length. The hypersonic boundary layer at $X \geq 1$ is described in a first approximation by a set of equations derived from Navier-Stokes equations with boundary conditions. Boundary conditions at the aft end of a body must be satisfied in addition to those near the leading edge. A complete set of boundary conditions was established in the form of a nonsingular solution. The conclusion was drawn that the flow at $M_1 \to \infty$ and $X \geq 1$ is described by the same boundary layer equations along the entire separation zone, except for small regions such as those near the angular points.

Zakharchenko, V. F., M. V. Tsvetkova,
and Ye. E. Borovskiy. Supersonic flow
around a porous cone. PM, no. 2, 1972,
132-134.

Supersonic air flow around a circular pointed cone with a
permeable surface was investigated in connection with the control of
incident heat flux and drag on streamlined bodies. Shadow photographs
were obtained of the unperturbed flow around a 0.197 rad half angle cone
at 0-0.24 values of the injection parameter $(\rho V)_1$, where ρ_1 and V_1 are
the density and velocity of the injected gas. The Mach number M_∞ of the
incident unperturbed flow was 2.9, the Reynolds number Re_∞/m was
2.6×10^6, and the ratio $T_{0\infty}/T_{01}$ of stagnation temperatures of the external
and injected gas was 1. Photographs were used to determine the angle Θ_s
between the compression shock front and the direction of the unperturbed
flow. It was assumed that the free stream boundary is also conic at uniform
gas injection through the conic surface and that the pressure along the
boundary is uniform. The boundary can then be assimilated to an impervious
surface of an imaginary cone as well as its position, i.e. the angle $\Delta\Theta$
between the boundary and the cone surface. Pressure p along the boundary
can therefore be calculated as in a problem of supersonic flow around a
cone. Calculations indicate that both Θ_s and $\Delta\Theta$ increase continuously with
increases in injection $(\rho V)_1$, the rate of increase depending on the $(\rho V)_1$
value. The pressure coefficient $\bar{p}_s$ on the boundary was calculated using
available data on supersonic flow around cones. Plots of the relative pressure
coefficient $\bar{p}_1 - \bar{p}/\bar{p}$ along the cone surface at different $(\rho V)_1$ values (Fig. 1)
show a qualitative pattern of variations of the pressure coefficient $\bar{p}_1$ in the
presence of air injection in comparison with the flow $(\bar{p})$ around an impervious
cone, i.e. in the absence of air injection. The experimental $\bar{p}_1 - \bar{p}/\bar{p}$ value
is shown (Fig. 2) to depend significantly on the coordinate x/L and $(\rho V)_1$.
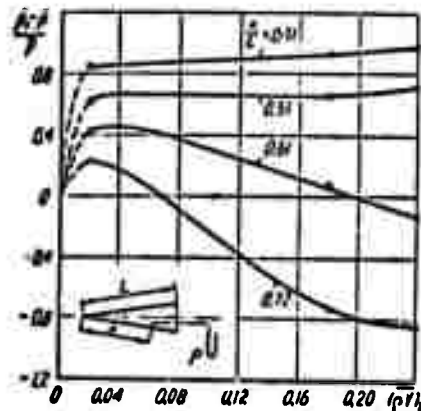

Fig. 1. Relative pressure coefficient
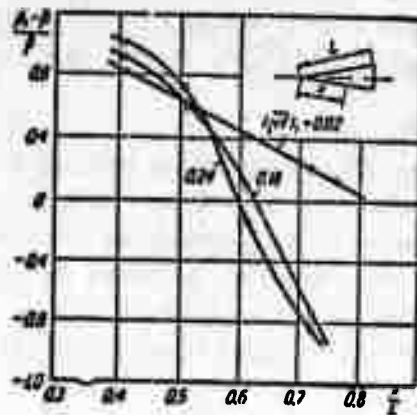versus injection parameter.

Fig. 2. Relative pressure coefficient versus coordinate x/L at fixed points of the cone generatrix.

The data reveal a significant dependence of incident flow parameters on the injection pressure and make it possible to calculate the drag on a permeable surface cone. Total drag calculations should include an allowance for injection drag which can amount to 10% of the total drag at a low injection pressure.

Lifshits, Yu. B. and E. G. Shifrin. On the problem of transonic flow over a convex corner. MZhiG, no. 2, 1971, 67-69.

Mathematical analysis of two-dimensional potential flow in the vicinity of the sonic point O shows that a similar solution, satisfying the conditions of Vaglio-Laurin's solution [J. Fluid Mech., 1960, v. 9, no. 1], is possible for equations of transonic flow over a convex corner. A solution to the $\psi(u, v)$ hodograph plane is obtained by analogy with that of Tricomi equations which become equal to zero at the $v = 2/3\ u^{3/2}$ characteristic of the first family of flow lines. A solution $C = |u|^3/v^2$ to the $\psi = 0$ equation was found in the third quadrant of the u, v plane. It is concluded that the profile in the subsonic region must be convex. A one-sheeted plot of the solution in the hodograph plane indicates that the sonic line is convex in relation to the region of subsonic velocities. The surface velocity vector at a transition point from the subsonic region is given by $u = (K^2C)^{1/3} \varphi^{2/3}$, where K is the curvature of profile in the O point. The similar solution derived satisfies a boundary condition in the vicinity of the salient point, as well as the condition of finite curvature in the subsonic region. The solution also describes the principal member of asymptotic expansion in axisymmetric and rotational flow.

I. A. Bogashchenko, A. V. Gurevich, R. A. Salimov, Yu. I. Eydelman. Flow of a rarefied plasma around a body. ZhETF, v. 59, no. 5, 1970, 1540-1555.

The structure of the disturbed wake behind a disc around which a rarefied plasma is flowing is studied in detail by the Langmuir probe technique. The plasma was produced in a Q-machine as shown in Fig. 1. Properties of the plasma flow are discussed. A characteristic radial distribution of quasi-neutral plasma is shown to exist, with maximal density around the system's axis. The distribution of ions in the plasma is given by
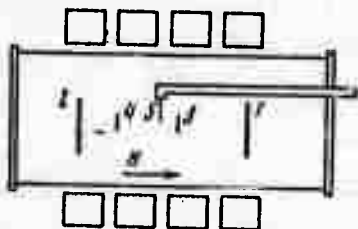

Fig. 1. Plasma generator.
1 - ionizer; 2 - anode; 3 - disc #1;
4 - disc # 2; 5 - test probe.

Maxwell's function; the anode potential is chosen so that the electron distribution in the plasma can also be given by the Maxwell function. The density, velocity and temperature in the plasma flow, surface potential and position of the disc were varied. Test measurements and their comparison with theory indicate the presence of ion acceleration in a selfconsistent electric field produced in the plasma. In the immediate vicinity behind the disc the effect of the electric field on ion motion is quite pronounced, causing a noticeable ion concentration near the axis. The plasma wake has a damped oscillatory profile; it is shown that the decrease of ionizer temperature and the increase of plasma density will increase the damping, and for $T \cong 1800^{\circ}K$ the distribution of plasma behind the body assumes an almost monotonic character. At large distances from the disc, plasma disturbance is shown to be a function of the radius only. An important role in oscillation damping is played by the deformation of the ion distribution function. The effect of ionic collisions on the ion distribution function is discussed in detail. An investigation of oscillation damping shows that the longitudinal and transverse ion temperatures gradually level out as a result of collisions. It is shown that the change of sign of the body potential relative to that of the plasma does not appreciably affect the structure of the disturbed wake behind the disc. However, a change of sign in the potential of another body located in the disturbed zone of the first body strongly affects the structure of the zone in the region between the bodies. Theoretical and experimental data are compared for the axial and radial plasma distribution in perturbed regions, and the results of the measurements are found in accordance with theory.

VII. ABLATION STUDIES

Karasev, A. B., and T. V. Kondranin. The
effect of ablation products on heat transfer
during destruction of graphite in radiative
air plasma. MZhiG, no. 1, 1971, 23-31.

A steady hypersonic flow of viscous, heat-conductive, radiating
air around the leading stagnation point of a graphite sphere is analyzed in
the region between the separated shock wave and the body surface. The flow
is described by a set of equations with self-similar variables and boundary
conditions behind the shock wave and on the surface. Heat transfer in the
radiant air was calculated by solving the equations by the method of successive
approximations. A binary model was adopted for diffusion of ablation products.
Chemical reactions were considered to be frozen in the boundary layer and
equilibrated at the boundary layer-shock wave interface. Gas state on the
ablation surface was determined from the chemical equilibrium condition,
assuming equality of vapor pressure with stagnation pressure. Radiative
and convective heat transfer were calculated in the presence or absence of
ablation. Analysis of plotted data shows that the spectral range of radiant
energy transfer is narrow in the streamline flow around an impervious surface
at high atmospheric reentry velocities. In the absence of ablation, the
total radiant heat flux changes insignificantly by transfer through a cold
boundary layer. Thus the presence at the boundary layer of ablation products
capable of absorbing or emitting radiation means that heat flow to the surface
will increase if the vapor product is opaque in the visible range, but will
decrease of opacity extends to $\lambda < 0.115$ micron. Actually, the shielding
effect at $\lambda < 0.115\mu$ is to a large degree cancelled by the radiative effect at
$\lambda > 0.115\mu$. A previous paper by these authors on graphite ablation was
published in Effects of Strong Explosions, no. 1, 1971, p. 41.

Karasev, A. B., and A. N. Lyakh. Study
of radiative and convective heat transfer
by an emissive mixture of carbon dioxide and
nitrogen flowing past the stagnation point.
MZhiG, no. 2, 1971, 39-47.

Hypersonic flow characteristics of a viscous thermally
conductive mixture (90% CO_2, 10% N_2) around a spherically blunted body
were calculated with allowance for radiation energy transfer and reabsorption.
Self-similar variables and boundary condition equations describe the gas
flow in a compressed thin shock layer, assuming local thermodynamic
equilibrium through the entire shock layer. A solution was obtained by

iteration and successive computation for flights of the spheres at 9,000 - 12,000°K and 1-10 atm pressure behind the shock wave. The spheres were of 1 m radius and had a 3000°K wall temperature. Analysis of resulting data revealed an insignificant radiation effect on convective heat transfer. The relative contribution of different spectral ranges to the radiative heat flux on the wall was found to be approximately 43, 40, 20, and 15% for the 0.128 - 0.33μ (CO band), 0.33 - 0.66μ (CN bands), 0.80 - 1.15μ and 0.45 - 0.80μ ranges, respectively. The contribution of the UV spectral range decreases while that of the visible range increases with an increase in pressure. Radiation heating is five times greater than convection heating at 10 atm and 12,000°K. Convective and radiative heat fluxes in the CO_2-N_2 mixture exceed the corresponding values in air by 20 and 40%.

Apshteyn, E. Z., L. G. Yefimova, and G. A. Tirsky. Intensive destruction of a vitreous body by [shock] radiation. MZhiG, no. 2, 1971, 131-134.

Destruction of a vitreous body by radiation from a shock layer in hypersonic gas flow is analyzed assuming an optically thin boundary layer at high injection rates and sufficiently intense vaporization. Presence of a liquid film near the stagnation point on the body surface is presumed, to simplify calculations of destruction parameters. Application of an approximation of radiative heat conduction in the body to the liquid film led to a set of transcendental equations which describe ablation, friction, and surface temperature as functions of shock layer parameters. Iterative solution of the equations is illustrated by diagrams of the destruction rate and gasification Γ of a heat insulating material with thermophysical characteristics of fused quartz under assumed flight conditions. Plots of Γ versus body radius R_B show that Γ decreases with a decrease in R_B due to liquid phase ablation. At great R_B values, coating destruction proceeds by vaporization only. The contribution of liquid phase ablation to the destruction rate becomes significant at small R_B, because of the effect of the radiative heat conductance parameter λ_R (Fig. 1). Since it increases greatly with increase in atmospheric reentry velocity, radiative heat flux is thus a decisive factor in calculation of destruction. A previous study on this problem was reported by Apshteyn in Effects of Strong Explosions, no. 1, 1971, p. 22.
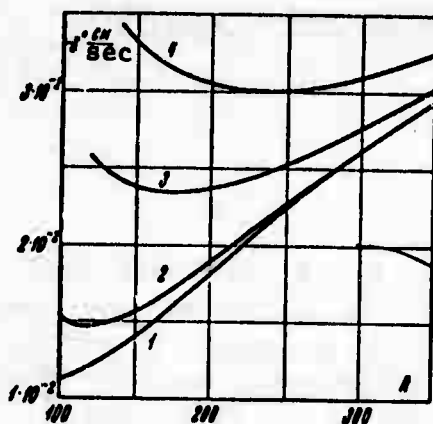
Fig. 1. Destruction rate of heat
insulating coating. Curves 1, 2, 3, 4
correspond to λ_R = 0, 10^4, 5 x 10^4,
10^5, respectively.

VIII. HIGH-PRESSURE EFFECTS

Vereshchagin, L. F., A. A. Semerchan,
N. N. Kuzin, and Yu. A. Sadkov. <u>Performance</u>
<u>of a three-stage high pressure unit with an</u>
<u>operational volume of approximately 100 cm^3.</u>
DAN SSSR, v. 202, no. 1, 1972, 74-75.

The performance characteristics are discussed of a high
pressure, three stage unit designed to produce large blocks of polycrystalline
diamond materials and composites based on synthetic polycrystalline diamonds.
These materials are suggested for the tooling of the main components of
another high pressure unit (with an operational volume of approximately
0.25 cm^3). The use of these materials, with superior physical and mechanical
properties, will lead to a substantial increase in the pressure range of the
0.25 cm^3 unit.

Pressures of up to 100 kbar can be realized with the 100 cm^3
unit. Calibration of the unit pressure scale was done using the reference
points of Bi_{I-II}, Ba_{II-III}, Bi_{III-IV}, and Sn; and also by the method of
electrical resistance using a 10,000 ton press. Concavity of the pressure
calibration curve is caused by a relatively small ratio (2:1) of F/F_1, where
F is the total force and F_1 is the effective first stage force. (F/F_1 ratio
is as much as 5:1 for the 0.25 cm^3 high pressure unit.) The increase of the
pressure range and the concavity of the pressure calibration curve are
dependent on an increase of the F/F_1 ratio, which is not attainable for the
100 cm^3 unit without a substantial increase in the second and third stage
cross-sections. Since larger parts made from the presently used cermet
hard alloy (VK-6) would likely suffer a loss in quality due to sintering, the
effective development of multistage units is predicated on fabricating at
least one of the stages using high strength steel.

The authors note that they have successfully produced large
blocks of polycrystalline diamond materials of the ballas and carbonado
types using the 100 cm^3 high pressure unit.

Vereshchagin, L. F., E. Ya. Atabayeva, and N. A. Bendeliani.
Phase diagram of Bi_2Te_3 at high pressures and temperatures.
FTT, no. 8, 1971, 2452-2454.

The phase diagram of semiconducting Bi_2Te_3 in the 40-85 kbar and 20-700°C ranges was plotted on the basis of the experimental isobars and isotherms of electrical resistance R. The R(P) and R(T) functions were measured mostly on single-crystal p - or n-type Bi_2Te_3 wafers in a high-pressure chamber designed at the Academy's Institute of High-Pressure Physics. Lithographic stone or AgCl were used as the pressure-transmitting medium. The boundaries of three high-pressure phases are shown on the P-T diagram of Fig. 1.
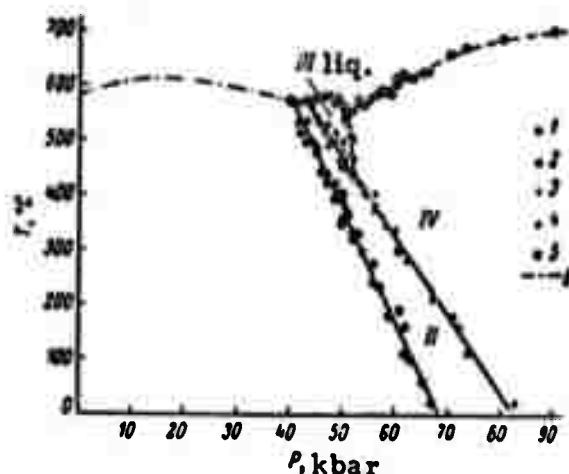

Fig. 1. Phase diagram of Bi_2Te_3.
1 - 4 - electrical resistance method,
5 - DTA method, 6 - data of D.L. Ball
(Inorg. chem., 1. 4, 1962)

The phase transition curves are described by the equations

$$P_{I-II} = 68.5 - 0.0493T, \quad P_{II-IV} = 82.8 - 0.0703T,$$
$$P_{II-III} = 84.0 - 0.0726T, \quad P_{III-IV} = 56.1 - 0.0094T, \tag{1}$$

and the P-T coordinates of triple points are tabulated (see Table I below).

Equilibrium	P, kbar	T, °C
Liq.+I+II	40.4	570
Liq.+II+III	43.0	566
Liq.+III+IV	50.9	553
II+III+IV	52.0	438

Table 1.

The I - II and II - III transitions are reversible; the II - IV transition is not reversible below 150°C. On cooling, the metallic phase IV yields a metastable phase at 20°C and 25 kbar pressure, intermediate between the phase IV and the original phase. The phase transitions detected are of the second order.

Kalitkin, N. N. and L. V. Kuz'mina. Cold compression curves at high pressures. FTT, no. 8, 1971, 2314-2318.

Pressure P, energy E of elastic compression of an atom, chemical potential, electron density ρ, and intra-atomic potential are calculated at 0° for each element of the Periodic Table. Calculations based on a quantum statistical model (QSM) are shown to be much simpler than the earlier calculations from the electronic spectra, and also more accurate than calculations based on the Thomas-Fermi model. The pressure P, as the other thermodynamic quantities cited, was expressed as a function of ρ, e.g.

$$P = \left[\frac{1}{5} (3\pi^2)^{2/3} \rho^{5/3} - \frac{1}{4} \left(\frac{3}{\pi} \right)^{1/3} \rho^{4/3} - \frac{\Delta\rho}{36} \right]_{r=R}. \tag{1}$$

where R is the radius of the Wigner-Seitz cell in the QSM. The tabulated P and E data for 13 elements and for atomic volumes v in the . 100 + 0 to .422 + 2 range were then calculated on a BESM-6 computer with a relative error in the -3 to +12% range. Analysis of the calculated numerical data with allowance for $\rho(r) \approx Z(v)$ at ultra-high pressures led to an interpolation formula P(Z,R) which, together with a formula analogous to (3) for a localizable P, were found to be sufficiently accurate. The P(v) curves of the mixtures and compounds can be plotted with the help of the cited formulas for P by solving the set of equations

$$P(Z_1, v_1) = P(Z_k, v_k), \ k > 1; \ v = \sum_{k=1} v_k. \tag{2}$$

which describe the equality of P in the cell of various components and the volume additivity, respectively.

Popov, V. N. and V. I. Chernyshov. Equation of state of a helium-nitrogen mixture. IAN Energ, no. 3, 1971. 162-165.

A procedure for statistical mechanical treatment of experimental compressibility data is described, to determine virial coefficients for He, N_2, and He-N_2 mixtures in the 273 - 773°K range of temperatures and at pressures to 400 bar. The virial coefficients B, C, D, E are given in polynomial form as functions of T. The coefficients of the polynomials are

tabulated. The virial equations of state for He, N_2, and He-N_2 mixtures were developed from the described treatment of the experimental data. The equation of state for a He-N_2 mixture where the index m refers to the mixture,

$$'m = 1 + ''mp + {}^Cmp^2 + {}^Dmp^3 + {}^Emp^4. \qquad (1)$$

describes the experimental results within $\pm$ 0.20%. Compressibility factors and density ρ values calculated from (1) were in satisfactory agreement with earlier experimental values over the experimental temperature and pressure ranges. This fact indicates that the caloric data calculated from (1) are sufficiently accurate and reliable for design of technological processes and solution of structural design problems.

Polyakov, L. M. **Effect of uniform pressure on the plasticity of rock salt crystals.** UFZh, v. 17, no. 2, 1972, 210-217.

Results are described of tests on the effects of uniform pressure on plastic deformation of rock salt crystals. The tests correlated pressure with the appearance of defects affecting dispersion and deflection of light, and also with threshold and type of destruction. An experiment was conducted with natural optically homogeneous rock salt crystals of 6 x 6 x 12 mm. Measurements of the intensity of light dispersion, i corresponding to the plastic deformation at given values of uniform pressure showed a peculiar process of destruction of NaCl crystals. In the beginning stage deformation takes place without a significant change in light dispersion; then at some deformation ϵ_{1p}, intensity starts increasing and at some further deformation ϵ_{2p}, the $i(\epsilon)_p$ curve reaches a saturation region, which finally concludes in the ultimate destruction of the crystal specimen at deformation ϵ_{3p}. The relationship between intensity of light dispersion and extent of deformation is shown in Fig. 1 with increase in uniform pressure, the intensity of light dispersion decreases, and its distribution in the crystal becomes homogeneous.

Fig. 1. Relationship between intensity of light dispersion, i and deformation stage ϵ:
1 - 0; 2 - 500 kg/cm^2; 3 - 1000 kg/cm^2;
4 - 2000 kg/cm^2; 5 - 3000 kg/cm^2; 6 - 5000 kg/cm^2.

The appearance of light dispersion coincides with the formation of crystal defects, dimension of which are significantly less than the wavelength of light (c ≈ 250-350 Å). In the case of a uniaxial compression, dispersion detectible at a deformation level $\epsilon_1 \approx 0.65\%$; if deformed under pressure of 5000 kg/cm^2, then deformation increases to $\epsilon_{1p} = 8.9\%$. Mathematical expressions are derived to determine the influence of pressure on plasticity and the value of deformation corresponding to light dispersion. The mechanism of destruction is described in detail and microphotographs are presented.

Fateyeva, N. S., and L. F. Vereshchagin. <u>Melting curve of molybdenum up to 90 kbar</u>. ZhETF P, v. 14, no. 4, 1971, 233-235.

A test is briefly described in which the melting curve of pure Mo under high pressure was measured by an optical method described earlier by the authors. The method is based on simultaneous determination of the radiation intensity ratios I_1/I_2 and I_2/I_3 of two pairs of narrow spectral regions, and their subsequent comparison with Planck's law. The experimental T(P) plots of Fig. 1 can be presented by the linear equation

$$T_M = 2883 + 0.8 \cdot 10^{-3} P \tag{1}$$

where T is melting point in °K and P is the pressure in bars. The probable error is ±% for both T and P measurements. A similar experiment was reported by Fatayeva et al on melting characteristics of graphite under high pressure [Explosion Effects Report No. 2, p. 58].
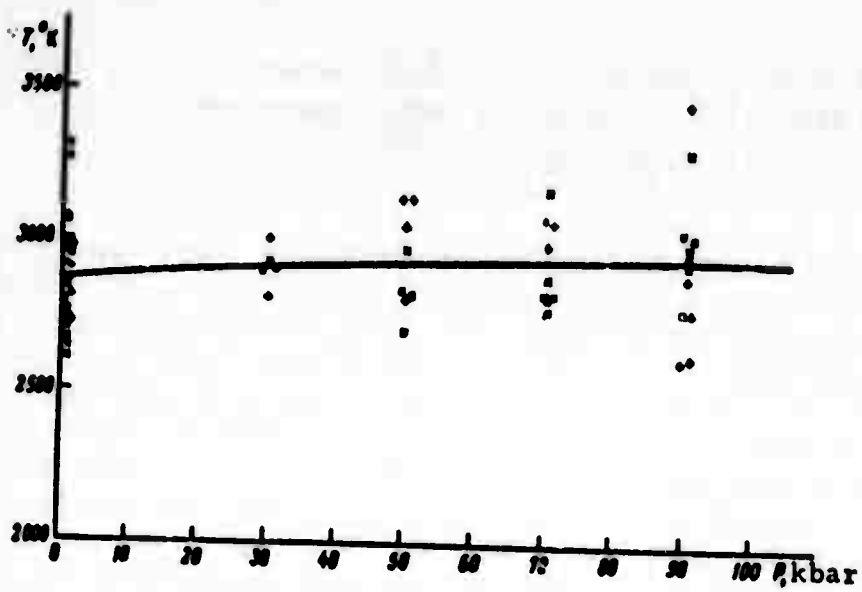
Fig. 1. Melting curve of Mo up to 90 kbar, calculated from all experimental points.
+ - temperature data of I_1/I_2 measurements,
x - temperature data of I_2/I_3 measurements.

IX. ELECTROMAGNETIC FIELD-PLASMA INTERACTION

Liberman, M. A., and A. T. Rakhimov.
Penetration of e-m waves into a plasma with
allowance for nonlinearity. ZhETF, v. 61,
no. 3, 1971, 1047-1056.

The authors examine the structure of an alternating electro-
magnetic field interacting with a weakly ionized plasma, for the case of
thermal nonequilibrium in the plasma. It is noted that nonlinear effects
begin to appear in such a case at relatively weak fields in comparison to
the characteristic plasma field. The discussion is limited also to the case
where the incident e-m field frequency is well above the electron-atom
collision frequency, but below plasma frequency. Using this model the
authors show that the effect of the e-m field on the local ion-recombination
balance in the plasma causes an appreciable change in the penetration
depth of the field into the plasma, according to the relation c/ω_p where ω_p
is electron frequency in the interaction region. Expressions are derived
illustrating the nonlinear decrement in e-m intensity with penetration, and
some sample calculations are given for the effect, using typical plasma
and beam parameters.

Golant, V. Ye. Wave penetration in plasma
at frequencies near the lower hybrid. ZhTF,
no. 12, 1971, 2492-2503.

Theoretical considerations are presented for optimizing the
introduction of e-m radiation into a magnetized plasma. It has been
shown that injection near the lower hybrid frequencies may be advantageous
since plasma opacity to the incident wave will be minimal here, to a wave
with correctly applied longitudinal delay. The author therefore investigates
the transformation region for frequencies near the lower hybrid, and
derives expressions for optimum energy transfer under these conditions.
It is assumed that the applied frequency lies well below electron cyclotron
resonance and well above ion cyclotron resonance. For the case of a
uniform applied magnetic field, expressions for optimal delay structure
parameters are obtained, assuming the idealized delay configuration
of Fig. 1. In some cases in a uniform field the requirements on delay
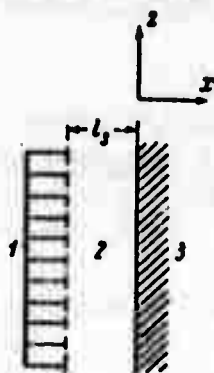
Figure 1. Delay geometry.
1 - delay element; 2 - vacuum;
3 - plasma.

parameters may become excessive; in that event a nonuniform external field may be applied, resulting in two transformation regions and simplifying the delay line operation.

X. IONOSPHERIC EFFECTS

Bykov, B. P., and S. I. Kozlov. Ion and
electron kinetics in a disturbed ionosphere
at altitudes of 100~200 km. Geomagnetizm
i aeronomiya, no. 2, 1972, 340-342.

Results are described of an investigation on kinetics of ions
and electrons at altitudes 100 < h < 200 km in a disturbe d atmosphere. The
disturbing action is assumed to significantly increase the degree of ionization
α of air, so that N_2^+, O_2^+ and O^+ are formed approximately in direct
relation to the N_2, O_2 and O contents at these altitudes. Investigation is
limited to values $\alpha \ll 1$, so it is considered that the atmosphere is not warmed
up due to a sharp rise of α, i.e. electrons, neutrons and ions of gas have the
high level of temperature distribution existing in normal ionosphere.

Form. no.	Reaction	Velocity const. cm^3 per sec
1	$O^+ + N_2 \to NO^+ + N$	$\alpha_1 = 2 \cdot 10^{-12}$
2	$O^+ + O_2 \to O_2^+ + O$	$\alpha_2 = 4 \cdot 10^{-11}$
3	$N_2^+ + O \to O^+ + N_2$	$\alpha_3 < 1 \cdot 10^{-11}$
4	$N_2^+ + O \to NO^+ + N$	$\alpha_4 = 2.5 \cdot 10^{-10}$
5	$N_2^+ + O_2 \to O_2^+ + N_2$	$\alpha_5 = 1 \cdot 10^{-10}$
6	$O_2^+ + N_2 \to NO^+ + NO$	$\alpha_6 < 1 \cdot 10^{-15}$
7	$O_2^+ + e \to O + O$	$\alpha^\circ(O_2^+) = 2.2 \cdot 10^{-7} (T_e/300)^{-1}$
8	$N_2^+ + e \to N + N$	$\alpha^\circ(N_2^+) = 3 \cdot 10^{-7} (T_e/300)^{-1/2}$
9	$NO^+ + e \to N + O$	$\alpha^\circ(NO^+) = 4.4 \cdot 10^{-7}(T_e/300)^{-1}, 200^\circ K \leqslant$ $\leqslant T_e \leqslant 500^\circ K$
		$\alpha^\circ(NO^+) = 0.9 \cdot 10^{-7}(T_e/1000)^{-1/2}, T_e > 500^\circ K$

Table 1.

The general scheme of elementary processes used in this work
and their velocity constants are given in Table 1. On the basis of these
reactions kinetic differential equations are obtained which were solved by
computer. Calculations are done for a wide range of altitudes and values of
N_{eo}, at day and night conditions. Results of calculations for daylight
conditions at $\alpha_3 = 10^{-11}$ and $\alpha_6 = 10^{-15}$ cm^3/sec are plotted. The main
characteristic features of ion and electron kinetics in a disturbed ionosphere
are seen to be as follows: 1) The role of N_2^+ ions is significant only at the
initial moment after disturbance, not exceeding in most cases ~1 sec;

2) At lower altitudes, as in a normal atmosphere, recombination takes place mainly according to a square law. However, with an increase of N_{eo} after the disappearance of N_2^+ over a certain time, velocity variation may follow a linear law. The duration of this time significantly increases at higher altitudes; 3) The time behavior of $[NO^+]$ differs little from predictions. Even at upper altitude regions, the role of this ion is small, except when $N_{eo} < 10^6$ cm^{-3}; 4) To a first approximation, at all altitudes the main molecular ion is O_2^+; 5) The principal difference in behavior of ions and electrons in night conditions from day consists in the fact that the dissociative recombination level increases, so that the role of N_2^+ and NO^+ ions substantially decreases; and 6) The decay time of electron concentration from N_{eo} to normal values of an undisturbed ionosphere has only a slight dependence on the value of N_{eo}.

These conclusions also hold up under varying values of the unknown velocity constants α_3 and α_6. All calculations were done assuming $\alpha_1 - \alpha_6$ to be independent of temperature.

Alimov, V. A. <u>Effect of strong radiowaves on the ionosphere</u>. Geomagnetizm i aeronomiya, no. 2, 1972, 346-348.

The author proposes possible mechanisms for increasing (or decreasing) electron density in a localized region of the ionosphere by means of a powerful r-f beam, and shows the considerable effect that such a beam may have on the nonuniform composition of the affected region. The analysis gives examples of the effects obtainable in terms of the D, E and F layers.

As is known, raising the electron temperature in a plasma may result in a drop in electron density N owing to ejection of plasma from the heated region, or alternatively N may increase owing to an upset of the ion recombination balance. In the first case N is established over a time $t_D \sim r_0^2/D_i$, where r_0 is the distance over which the excitation wave amplitude changes significantly [sic], and D_i is the ion diffusion coefficient. In the second case, N is determined by the lifetime of a free electron, $t_e \sim (\alpha' N_0)^{-1}$, where α' is the effective coefficient of electron recombination and N_0 = original unexcited density.

Therefore, for $t_D < t_e$ the plasma ejection process is dominant, e. g. for the upper portion of the F-layer, where

$$N = N_0[1 + (E(r)/E_p)^2]^{-1}, \qquad (1)$$

in which E = amplitude of the excitation wave and E_p = plasma field, as defined by Gurevich[1]. Conversely, when $t_e < t_D$ the recombination process dominates, as in the lower ionosphere where

$$N = N_0[1 + (E(r) / E_p)^2]^{1/4}. \qquad (2)$$

Using standard parameters for the F-layer and assuming $r_o < 300$ km, Alimov shows that Eq. (1) applies; for the E-layer at $r_o > 0.1$--1 km, Eq. (2) would apply. In the latter case it must be emphasized that (2) is valid only for a concrete relation of α' to electron temperature T_e. This applies in the E-layer, but at present it is not possible to assert a definite α' (T_e) for the D-layer.

A brief consideration of the effect of ionospheric drift on excitation lifetime shows that drift effect is negligible on the steady-state component of the excited region, providing the excitation rate is sufficiently larger than normal decay. This is the case, for example, in the E- and F-layers for $r_o > 7$ km.

Besides changing the gross level of N in the foregoing manner, the r-f excitation also affects the fluctuating component. Thus in the E-layer the mean square fluctuation in electron density will increase by

$$\overline{(\Delta N)^2} = \overline{(\Delta N_0)^2}[1 + (E(r) / E_p)^2]^{1/2}, \qquad (3)$$

and in the F-layer will decrease by

$$\overline{(\Delta N)^2} = \overline{(\Delta N_0)_0^2}[1 + (E(r) / E_p)^2]^{-1}. \qquad (4)$$

The turbidity of the excited region is then shown to be a function of r-f field, where turbidity factor α is given by

$$u = \frac{P_s}{P_0} = 1 - \exp(-\bar{s}^2). \qquad (5)$$

in which P_0 is incident energy, P_s is scattered energy, and $\bar{S}^2$ is mean square phase fluctuation in the layer. Using an earlier notation[2] for transmission of r-f through the layer, namely $\bar{S}^2 = \bar{S}_0^2 (\Delta N)^2/(\Delta N)_0^2$, the author obtains graphical solutions from (3), (4) and (5), showing the effect of applied field on turbidity. These are given in Fig. 1 for the E- and F-layers respectively, and show the considerable effect of incident r-f field. This appears particularly
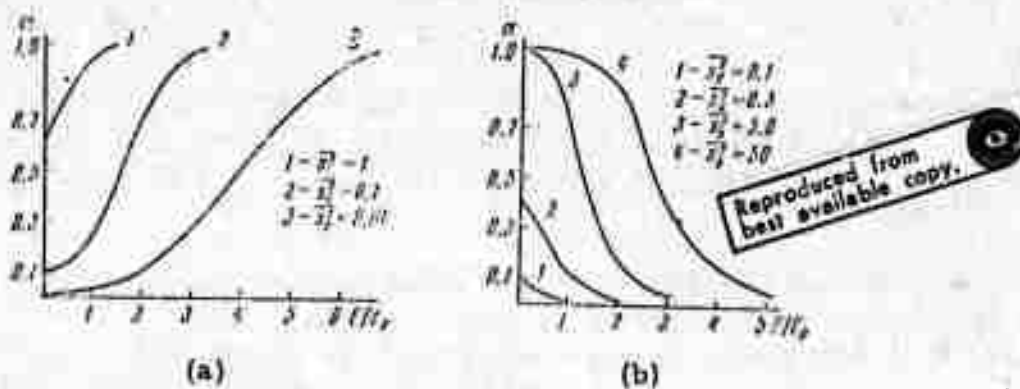
Fig. 1. Turbidity factor variation with
applied field for E-layer (a) and F-layer (b).

significant for the F-layer, since there the turbidity effect is sharply reduced at
sufficient transmitted power, tending to nullify the disturbance effect.

References

1. Gurevich, A. V. Geomagnetizm i aeronomiya, v. 5, 1965, 70;
   v. 7, 1967, 291.
2. Alimov, V. A., et al., ibid., v. 11, 1971, 790.

XI. RADIATION DAMAGE

Brudnyy, V. N., V. P. Voronkov, M. A. Krivov,
and S. V. Malyanov. Effect of electron radiation
on gallium arsenide photodiodes. IVUZ Fiz, no. 1,
1972, 106-107.

Results are reported of an investigation on characteristics of gallium
arsenide photodiodes after radiation by electrons with 1.5 MeV at 300°K. Experiments were done with diodes having a base thickness of 120, 130 and 520 microns
at radiating flux densities of 0; $1.1 \times 10^{15} cm^{-2}$, $2.2 \times 10^{15} cm^{-2}$ and $3.3 \times 10^{15} cm^{-2}$.
In all cases the volt-ampere, spectral, and luminescence characteristics were
graphed for conditions before and after irradiation (four characteristic curves
are given). Comparison of the curves shows a significant change in the characteristic
of photodiodes after radiation, particularly in the forward v-a characteristic.
The authors recommend taking these effects into account during operation of such
devices in a radiation field.

Vorob'yev, A. A., O. B. Yevdokimov, and N. P. Tubalov,
Tomsk Polytechnical Institute imeni S. M. Kirov.
Effect of Overcharge of a Dielectric Charge by an
Electron Beam. Leningrad, FTT, no. 12, Dec. 1971,
3691-3692.

It is shown for the first time that a change in the sign of the
effective space charge can occur in plexiglass in the course of time. It is
noted that it was known that a negative space charge of thermally insulated
electrons is produced upon the irradiation of high-ohmic dielectrics by fast
electrons, and this appears in the development of discharge diagrams and is
applied in studying the electrical properties of dielectrics. Plexiglass
discs 4.5 mm thick and coated with 5-micron aluminum foil were irradiated by
0.8-1.2 Mev electrons at a current density of 0.5 $\mu amp/cm^2$ for 15-20 sec, and
then the space charge was tested using the effect of an electric field on the
passage of beta particles through a dielectric. The charge samples were
periodically irradiated by beta particles from a strontium-iridium source,
and the number of passing beta particles was measured. The figure is given
showing the relative change in the number of passing beta particles due to
the electric field as a function of time after irradiation. The figure shows
that the change in sign of the effective space charge is observed if the
maximum in the distribution of the stopped electrons shifts to one of the
surfaces of the plate. In this case a positive space charge arises in the
region of the dielectric not occupied by the negative space charge due to
injection from the surface. Overcharge is attributed to leakage of the negative space charge more rapidly than leakage of the positive space charge.
The observed overcharge effect is related to the electric state of the plexiglass, just as in polystyrene, which, as distinct from plexiglass, does not
yield an electric state and overcharge is not observed.

XII. LASER EFFECTS ON MATERIALS

Avotin, S. S., E. P. Krivchikova, I. I. Papirov, P. I. Stoyev, and V. I. Tereshin. Change in electrical resistance of beryllium from laser radiation. ZhETF, v. 62, no. 1, 1972, 288-293.

Transient and long-term effects of laser irradiation on resistivity of beryllium are described. Tests were run on 0.2 mm thick Be foil strips, exposed to pulsed radiation from a GOR-100M laser (not identified) generating 1 millisecond pulses at 40 j, focused to a 2.5 mm dia. spot on the foil surface. Resistivity ρ was measured during and after exposure with a constant 1 a current passed through the specimen. Variation of ρ during exposure is illustrated in Fig. 1, with calculated values of local
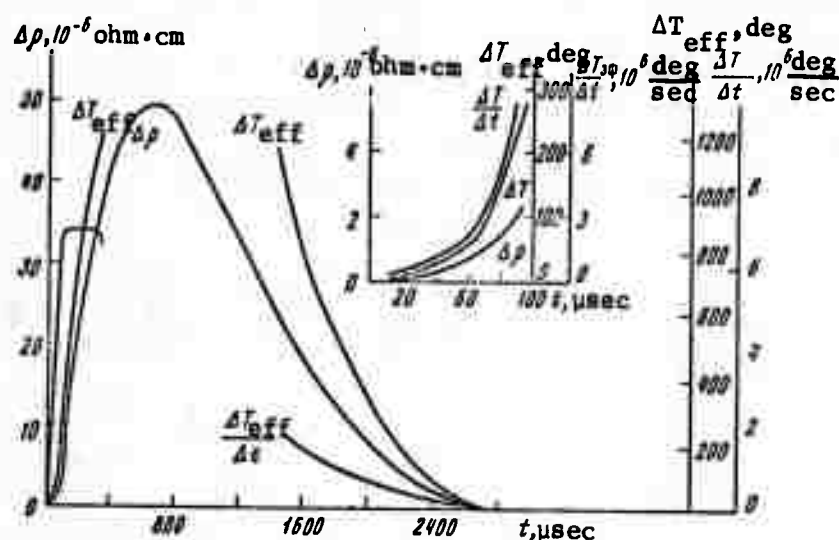

Fig. 1. Resistivity variation in laser-irradiated beryllium.

temperature rise ΔT_{eff} also included. A detailed examination shows three distinguishable stages in $\Delta \rho(t)$ up to the 700 μsec point, as indicated by the curve form. In the initial stage ($< 100 \mu s$) a local heating rate of about 10^6 deg/sec was calculated to exist in the impact region. It is noteworthy that a full anneal back to pre-exposure values of ρ occurs when the test is done in a 300°K ambient, whereas at 77°K, ρ continues to increase for an interval following irradiation, and after several hundred microseconds levels off at a value some 9% above the original value. The latter effect is ascribed to an increase in structural defect density during the high temperature anneal.

Belozerov, S. A., G. M. Zverev, V. S. Naumov, and V. S. Pashkov. <u>Destruction of transparent dielectrics by radiation from a mode-locked laser.</u> ZhETF, v. 62, no. 1, 1972, 294-299.

A comparative test was made on damage thresholds in various dielectrics from pulsed laser radiation. The main purpose was to illustrate the difference in effect of single pulse (10 ns) and a train of short pulses (30 x 4 ns) from a mode-locked Nd laser on dielectric breakdown. The test materials included type K-8 glass, fused and crystal quartz, leucosapphire, and ruby with and without color centers. The test conditions and findings generally duplicate those of Orlov et al (<u>Effects of High Power Lasers,</u> Dec. 1971, p. 49), who also advised on the present experiment. A typical filamentary breakdown in the short-pulse regime indicated self-focusing, evidently not thermal, which was not apparent in the monopulse regime. The tests verify that while energy densities for threshold are of the same order of magnitude for all dielectrics tested, the power density threshold for the short-pulse mode is typically several orders higher than for the 10 ns monopulse, and was found to go as high as 10^{14} w/cm^2. This suggests a thermal relief mechanism operating between pulses in the pulse train case. Photos are also included comparing filament appearance of the ruby with color centers to that in the remaining specimens.

Zverev, G. M., Ye. A. Levchuk, V. A. Pashkov, and Yu. D. Poryadin. <u>Optical destruction of the surface of lithium niobate.</u> ZhETF, v. 62, no. 1, 1972, 307-312.

Anomalous breakdown thresholds of laser-irradiated LiNbO$_3$ are examined and the types of destruction mechanisms taking place are suggested. In contrast to most dielectrics, LiNbO$_3$ has both a markedly lower breakdown threshold at room temperature, as well as a distinctly irregular change in breakdown level with increase in ambient temperature. This was observed in radiation tests with a focused Q-switched Nd glass laser at 1.06μ on polished LiNbO$_3$ specimens, in which 20 ns, 0.1 j pulses were applied at f = 15 cm. Threshold at room temperature (120 Mw/cm^2) increases with ambient temperature as seen in Fig. 1, exhibiting step jumps at the Curie points. In contrast, the threshold characteristic of LiTaO$_3$
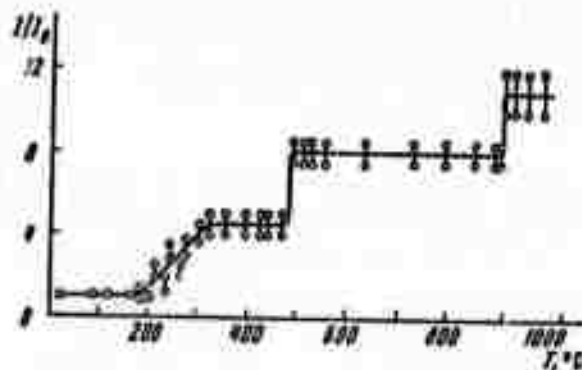
Fig. 1. Relative threshold intensity vs. temperature, LiNbO$_3$.

and BaTiO$_3$ were found to have no temperature dependence until the Curie point was reached, while for ruby and glass, no temperature dependence of threshold could be found between 20--700°C. At lower temperatures a cumulative effect of laser pulses on threshold is also noted in LiNbO$_3$ which is shown in Fig. 2. An analysis of these findings
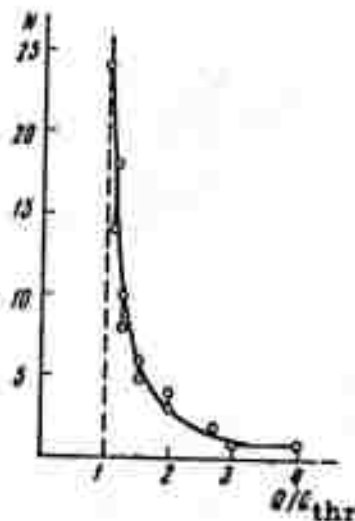

Fig. 2. Relative threshold vs. total laser pulses, N.

indicates that for temperatures below 330°C, surface damage is a function of light absorption in small trapping centers, whereas at higher temperatures the predominant mechanism is absorption by free carriers in the surface layer.

Uglov, A. A. <u>Work presented in the seminar</u>
<u>on the physics and chemistry of materials</u>
<u>processing by concentrated energy beams.</u>
FiKhOM, no. 5, 1971, 158-159.

Highlights are given of selected papers in the 27th Seminar
on the title subject, held in Moscow during February, 1971. The seminar
was chaired by Academician N. N. Rykalin, and attended by over 80
leading researchers in the field from Soviet institutes. The bulk of the
articles deal with high-power laser interaction with metal and dielectric
targets, CO_2 lasers being most often mentioned. To a lesser degree,
particle-beam interactions are also discussed.

A paper by V. P. Veyko et al discussed the growth kinetics of thin
oxide films on metals from pulsed heating, and methods for optimizing
film control. Experiments with a c-w CO_2 laser have yielded a 40-50 Å
oxide film on chrome at 1 millisec exposure, which is consistent with
calculated values. A number of test results by the same authors on poly-
mer targets was also discussed.

A. E. Kuznetsov et al presented their findings on vaporization
of dielectrics by 10.6 micron laser radiation, using quartz and other
optical glass under c-w CO_2 exposure. From their results the authors
have developed an approximate mathematical model based on the law of
mass conservation. Commenting on this, Yu. N. Lokhov noted the similarity
in characteristics between CO_2 destruction of dielectrics and the self-con-
sistent damage mode of metals under giant pulse exposure.

A paper by I. G. Stolyanova et al discussed aspects of laser
milling techniques in microelectronics; the authors have developed a
technique for producing laser-cut thin film resistors.

An interesting report by M. S. Baranov et al described computer
and experimental studies on the effect of laser pulse envelope in beam-target
tests. Results with rectangular, triangular and approximately sinusoidal
waveforms showed maximum metal vaporization for the triangular waveform
and minimum for the half-wave sinusoid. A criticism offered here by
A. A. Uglov, which applied generally to the laser beam-target tests, was
that attention tends to focus only on the strictly thermal effects occurring,

whereas chemico-thermal mechanisms also play a part and warrant more detailed examination.

Techniques for electron beam processing of materials are mentioned by A. N. Kabanov, D. B. Zvorykin et al, and Yu. D. Belotovskiy et al. These concerned nonthermal beam processing, electron lithography, and beam deposition techniques for metal films.

In summary, Dr. Rykalin observed that advances in laser tunability are needed to expand laser processing techniques, and that more detailed study of chemico-thermal processes is needed for both laser and particle beam techniques.

Anisimov, S. I., and V. I. Fisher. Ionization relaxation and light absorption behind a strong shock wave in hydrogen. ZhTF, no. 12, 1971, 2571-2576.

A simplified analysis is presented which describes the effect of ionization kinetics behind a shock wave on e-m radiation absorption in this region. The model assumes a plane stationary shock wave, and limits the consideration to hydrogen, since this avoids the complications of multiple ionization. The ionization relaxation zone in the shock wave wake is divided for analytical purposes into two regions with differing mechanisms of free electron formation: (1) a region of "seed electron" formation from atom-atom collisions; and (2) an electron avalanche region, with electrons freed predominantly by electron-atom collisions. Most of the optical absorption, as well as the significant change in gas state, occurs in region (2), which is therefore the region mainly treated in the paper. Equations for incident flux density and degree of ionization are numerically integrated, together with equations for one-dimensional stationary flow of the gas. The calculated results of density and temperature profile, together with ionization characteristics, are shown to have a definite correlation with incident flux density. The authors emphasize that the characteristics of hydrodynamic variables in such a shock wave, i.e. one absorbing an intense optical flux, will differ from the corresponding parameters in the usual detonation wave, owing to the ionization relaxation region which will exist in the former case. Some graphical solutions of the results are included.

Norinskiy, L. V. **Initiation of a controlled**
breakdown in gas by third-harmonic emission from
a neodymium laser. IN: Kvantovaya elektronika.
Sbornik. Moskva, Izd-vo Sovetskoye radio, no. 5,
1971, 108-109.

An experiment is described which was an extension of work
by Ákmanov et al (ZhETF P, v. 8, no. 8, 1968, 417), in which a directional
breakdown in gas was triggered by u-v laser radiation at 4.7 ev photon
energy and 300 Mw/cm^2 density. The present author has duplicated the
effect in atmospheric air, obtaining a controlled breakdown from the third
harmonic of an Nd glass laser at 3.5 ev. A collimated 3rd harmonic beam
was passed through slotted high-voltage electrodes which were 1 cm apart,
to obtain the controlled breakdown effect. Power density in the gap was
about 3Gw/cm^2, or two orders less than natural optical breakdown. Attempts
to repeat the effect at the fundamental and second harmonic were unsuccessful
since breakdown threshold was first exceeded in both cases. The results
confirm the inability of the fundamental (1.17 ev) and second harmonic
(2.34 ev) to generate the controlled breakdown condition owing to their
insufficient photoionization levels. Norinskiy emphasizes that his results
were obtained with a multimode laser, and should be repeated with a
single-mode regime for better clarification of this phenomenon.

Kaytmazov, S. D., A. A. Medvedev, and A. M.
Prokhorov. **Effect of a 400 koe magnetic field**
on the plasma of a laser spark. ZhETF P, v. 14,
1971, 314-316.

An experiment is briefly described in which the controlling effect
is studied of an external magnetic field on the geometry of a laser spark
plasma. Two conditions must evidently be met for field control of spark
geometry, namely (1) field pressure must exceed gas kinetic pressure
in the plasma, and (2) the skin layer should not exceed spark radius, r.
This means that the external field must be sufficiently great that on
lowering of plasma pressure to the magnetic pressure level, plasma
temperature still remains high enough to preclude diffusion in the external
field. The corresponding threshold for field control in the present case
was calculated to be on the order of 300 koe. Tests to corroborate this
were run at levels up to 500 koe, using a transformer-fed one-turn coil
of 0.8 cm dia. instead of the usual capacitor bank. A 100μsec field pulse
was thus generated, which simplified the requirement of exact synchro-
nization of laser spark and field pulse. Tests were run in ambient air,
using a neodymium glass laser at 2--3 j in both giant pulse and spike
regimes to produce breakdown. The comparative effect of the field is
seen in Fig. 1, where the spark is confined to a cylindrical form with

Fig. 1. Field effect on laser spark. a, c - no applied field; b - field applied

a smooth boundary. In both laser regimes the field increased spark axial length by about 1.5 times; it follows that this formation should retard plasma cooling. Nominal spark parameters of $r = 0.1$ cm and time constant $\tau = 3 \times 10^{-7}$ sec led to the conclusion that the plasma temperature attained was at least 6×10^5 deg. K.

Afanas'yev, Yu. V., and V. B. Rozanov.
Spectrum of multiply-charged ions in a laser
plasma. ZhETF, v. 62, no. 1, 1972, 247-252.

A physical model is proposed for the energy spectral form of multiply ionized atoms in a laser plasma. Based on certain assumptions regarding plasma diffusion, the model permits the development of an analytical expression which describes the desired ion energy distribution. The analysis demonstrates that a principal factor governing the energy spectrum for a range of Z-charged ions is the recombination process during the diffusion period following termination of the laser pulse. It is furthermore shown that the set of Z present at the end of the pulse does not necessarily contain all Z values present following this time. For simplicity a spherically symmetrical plasma flare is assumed to exist

at pulse termination, expanding into a vacuum according to a self-similar law. The energy spectrum is then derived as a function of initial flare density N_0 and time. Assuming values of $N_o = 10^{20}/cm^3$, temperature $T = 100$ ev and $Z \cong 20$, the authors find a characteristic photorecombination time $\tau_{pr} \cong 3 \times 10^{-10}$ sec, which is less than plasma diffusion time, hence the recombination effect can be appreciable. Analogous experimental work of Bykovskiy et al is cited (ZhTF, 1970, 2578, and ZhETF, v. 60, 1971, 1306), but lack of complete data from the latter preclude a useful comparison of theory with experiment. A more recent similar work of Mattioli is also cited (Plasma Physics, v. 13, 1971, 19) in which decay of an LiH plasma was calculated from ionization and recombination processes.

Yevtushenko, T. P., V. Kh. Mkrtchyan, and G. V. Ostrovskaya. Spectroscopic studies of a laser spark. IV. Absorption spectrum of a spark in hydrogen. ZhTF, no. 12, 1971, 2581-2589.

This is the fourth report in a series by the authors on laser spark spectroscopy; the previous article was reported in Effects of High Power Lasers, Dec. 1971, p. 7, on spark spectra in air, He and Ar. In the present tests the absorption spectrum of hydrogen at 6 atm was measured and compared to the continuous spectrum of an air breakdown. The same method was used as in the earlier tests, as shown in Fig. 1, using two Nd glass lasers to generate the sparks. The lasers were identical
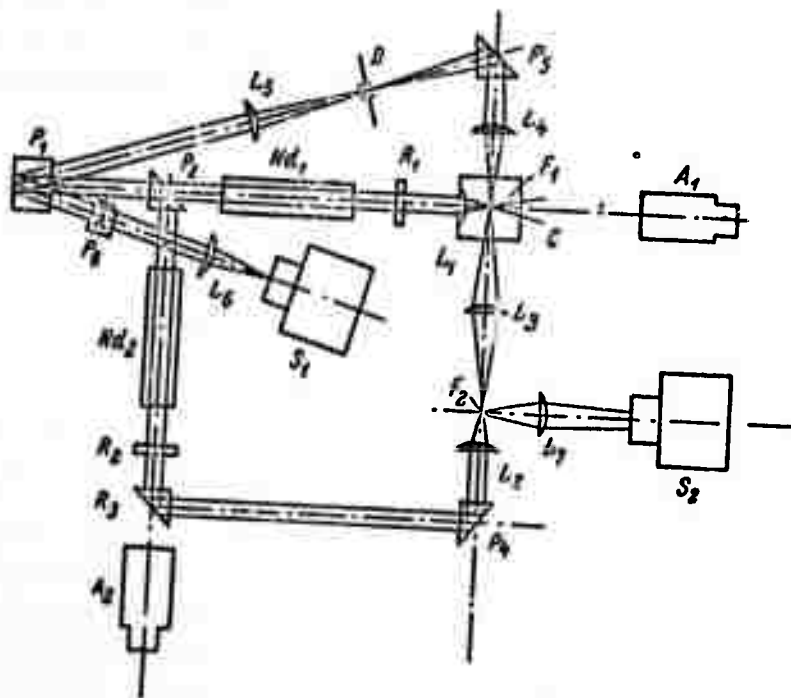

Fig. 1. Schematic for spectral study of a laser spark in hydrogen. A_1, A_2 - monitor tubes; C - hydrogen vessel at 6 atm; F_1, F_2 - sparks; S_1, S_2 - spectrographs.

and developed giant pulses of 0.5 j using a driven prism Q-switch rotating at 27,000 rpm. A large amount of graphical data on spark parameters, deduced from the spectral response, is presented and analyzed including the time characteristics of absorption, N_e, and plasma temperature. An example is given in Fig. 2, showing temperature, pressure and density variation in the center of the spark. In conclusion
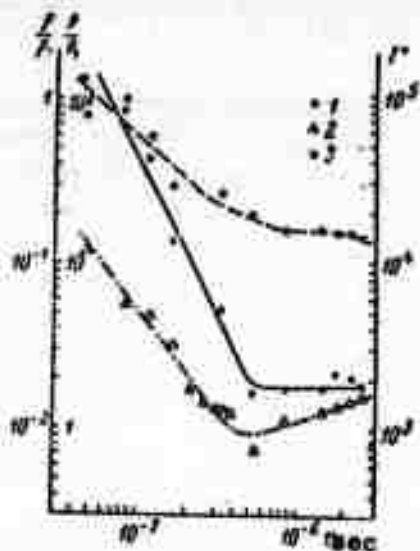
Fig. 2. T, p, ρ (t) in the center of a laser spark in hydrogen. 1 - pressure; 2 - density; 3 - temperature.

the authors discuss the accuracy of the spectral method for deducing the cited spark parameters.

XIII. MECHANO-ELECTROMAGNETIC EFFECT

Tyurikova, L. A., B. G. Averbukh, N. I. Moskvitin, and N. A. Krotova. Study of the parameters of r-f radiation from breakdown of a polymer bond to a solid. DAN SSSR, v. 201, no. 4, 1971, 833-836.

The relationship of adhesion mechanical properties to r-f radiation parameters in film + steel and film + glass bonds was studied under atmospheric conditions. The films were: KLT polymer (a mixture of polyethylene terephthalate and natural rubbers), adhesive plaster, cellulose esters, and PVC. An experimental apparatus was used to: (1) strip the polymer film at a variable rate, (2) measure the energy of adhesion and duration of film stripping as well as emitted r-f pulse length; (3) photo record radio signals; (4) determine emission frequency; and (5) study the shape and estimate the length of the r-f pulses. The radiation detector (Fig. 1) permitted observation of pulses with a rise time of at least 0.1 sec.
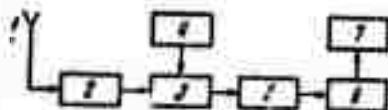

Fig. 1. Diagram of radio wave recorder:
1 - antenna, 2 - input circuits, 3 - mixer,
4 - heterodyne, 5 - I-F, 6 - detector,
7 - oscilloscope.

Sensitivity was $30 \mu V$, transmission band width was $\Delta f = 10$ kHz, and the intermediate frequency was $f = 460$ kHz. A 1 m telescopic antenna was placed at a maximum distance of 1.5 m from the film separation opening.

Pulsed radiation of a minimum 1 MHz frequency was detected during stripping of all of the films, with the exception of cellulose esters. A pulse was detected however, during the instantaneous separation of a cellulose aceto-butyrate film from glass. The rate of stripping consequently is a definite factor in the generation of r-f. The intensity I of radiation increases with an increase of discharge current from the electrical double layer. This was confirmed by an
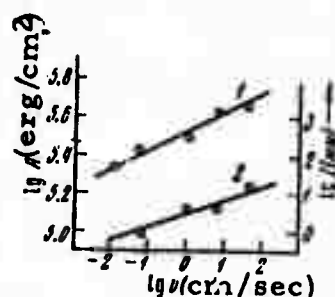
Fig. 2. Energy A (1) and radiation
intensity I (2) versus peeling rate v of
a KLT rubber film from a metal.

experimentally observed increase in pulse amplitude with increases in stripping
rate v. At a given v, I is higher when adhesion is stronger (Fig. 2). The
magnitude of I in film separation from metal is lower than in dielectric separation.
An oscilloscope trace of 10 MHz radiation during stripping of a KLT film from
a dielectric, e.g. glass, at v = 1 m/sec shows high-amplitude periodic pulse
packets in addition to smaller amplitude pulses. The period T between high
amplitude pulses is constant, i.e. dynamic resistance is constant for a given
gas and gas pressure. Electromagnetic phenomena observed in adhesion
breakdown generally follow the same pattern as in a gas discharge, but also
display certain unique characteristics. The presence of the interval T is related
to accumulation of a static charge along a considerable portion of the stripped
film; surface electrical conductivity must thus play an important part in
adhesion breakdown. The time dependence of radiation amplitude remains uniform
within a 1-10 MHz range of frequencies. Radiation intensity oscillations in sectors
of small and high-amplitude pulses reveal the discrete nature of discharges
which occur in microregions of a stripped film, where field intensity is critical.

In agreement with earlier findings, the length of an elementary
stripped region of rubber film on glass was determined to be 300μ. Generation of
r-f oscillations is considered to be the most convincing proof of gas discharge
development in a propagating crack. Visible radiation and acoustic vibrations
were recorded along with r-f in all cases. At stripping rates of 0.1 - 1 cm/sec,
the visible and r-f pulses were synchronized as determined from an oscilloscope
trace of rubber film stripping at v = 0.1 cm/sec. Oscillatory emission of
"mechanoelectrons" was also observed during adhesion breakdown in vacuum.
This confirms the oscillatory nature of the breakdown and associated phenomena.

Experiments are described which were designed to test hypotheses on the magnetohydrodynamic origin of radiation emitted by rapid mechanical deformation and rupture of metals. The particular case considered was for an impact velocity $V \approx 1,000$ m/sec and in the absence of an electric field. Radiation in the 3,000 - 8,200 Å range was not reliably detected in preliminary measurements of rupture of Cu, Al, Mo, and Bi samples using an impact testing machine at V = 7 m/sec. Other tests at V up to 1,200 m/sec were done by the technique of "contactless" rupture of a sample (1) separating two cylindrical chambers (2) and (3) as shown in Fig. 1a. Pressure was maintained at 1 torr in chamber (2) and at $10^{-3} - 10^{-2}$ torr in chamber (3). Deformation or rupture of the rear side surface (1) which closes chamber (3) was initiated by a 15 mm dia copper impactor (4). Radiation in the 3,000 - 8,200 A range was recorded by a photo-multiplier (6) through window (7). A copper deformation rate of about 100 m/sec was determined from x-ray shadow photographs taken at regular intervals.
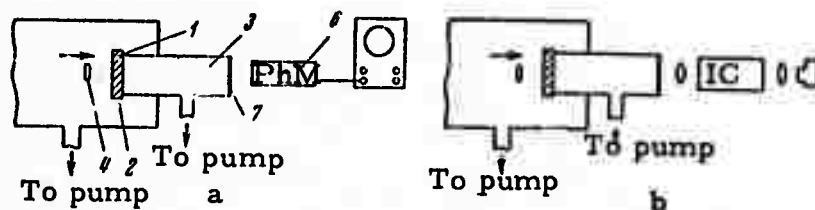

Fig. 1. Experimental configurations.

Rupture of the rear surface was accomplished in 112μsec. At a 1200 m/sec impact velocity, oscilloscope signal traces from the photomultiplier show 2-2.5 msec pulses with several characteristic peaks. Pulse intensity from a ruptured copper surface was 3-8 times that from a deformed surface without any visible rupture. The radiation pulses were recorded with 27 and 33 mm thick samples. In one control experiment, a 50 mm thick sample was not deformed and no radiation was detected. A special control experiment was set up involving exclusion of triboluminescence of the oxide film. In this experiment, a supposedly oxide-free copper surface formed on the rear face of a 27 mm thick sample by a previous impact was reimpacted 2-3 min after the first impact. A light pulse of the same intensity, but shorter than the first one, was recorded in this experiment. In both experiments, radiation from collision or friction of the sample with the small chamber walls did not interfere with the recordings, because the colliding and friction parts were shielded from the photomultiplier. Residual gas interference in the shock wave front was also excluded, since a shock

wave could not develop at subsonic deformation velocities. No trace of crack edge melting was detected on the photographs, indicating that thermal radiation was recorded. Analogous results were obtained in experiments with duralumin. Final proof of radiation emission from the part of the sample in the process of deformation and rupture was obtained by photographing the self-radiation of a luminescent crack in copper using an image converter (Fig. 1b). The radiation contour in the photograph coincides closely with the crack contour.

It is concluded that the experimentally observed radiation is emitted by deformation and rupture of the metal. This radiation exhibits the principal characteristics of luminescence, i.e. it exceeds thermal radiation at a given temperature, and its lifetime exceeds significantly the period of a light wave.

XIV. MISCELLANEOUS

An electronographic analysis of graphitization kinetics in thin amorphous carbon films exposed to powerful light pulses was performed. The optical source in this case was an IFP type xenon flashlamp, operating at voltages up to 1.7 kv. Carbon films were obtained by thermal diffusion of carbon rods onto cold glass substrates; samples were then placed on a copper grid and exposed to various energy light pulses, and in this manner various stages of graphitization were obtained. Kinetics of graphitization was studied from the nearest order parameters, which were determined for each graphitization stage from the radial atomic distribution curves. Radial atomic distribution curves were calculated from the electronograms obtained by means of an electron microscope and processed according to techniques described by I. D. Nabitovich et al. (Kristallografiya, no. 4, 1967, 584.) Experimental data and theoretical calculations indicate that there is a definite similarity in the structure of amorphous and graphitized carbon films. Amorphous carbon has a partially ordered hexagonal lattice structure, similar to that of the graphite crystalline lattice. However, there are different atomic layer arrangements in amorphous carbon and graphite. Based on the analysis of the structure of original amorphous carbon films and radial atomic distribution curves, the authors suggest the following graphitization kinetics. During the first graphitization stages a certain number of carbon hexagons with a single C-C bond are destroyed. Predominantly double and triple carbon bonds are formed among the released carbon atoms. During the subsequent graphitization stages the hexagonal and structural ordering takes place. The atomic layers are formed in such a manner that every atom has one neighbor in the adjacent layers. (In amorphous stage every atom has on the average four neighbors in adjacent layers.) In the final graphitization stages the hexagons get somewhat distorted; however, there is no change in relative positions of the atoms. It is suggested that the cause for the hexagonal distortion is the formation of double carbon bonds between certain adjacent carbon atoms, which thus coexist with single carbon bonds in the final graphitization stage.

Zaytsev, A. V. A new theory of ball
lightning. ZhTF, no. 1, 1972, 213-216.

The author expounds a theory of ball lightning formation based
on published research data on the formation of extremely fine electroconductive
structures in an electric field. Such structures are composed of fine metallic
or partly burned ash and soot particles. Analogous structures combined with
a corona space charge may form a streak lightning embryo. Discharge current
from the structure in a static earth - cloud electric field flows through the
structure resistance and heats it. The heated structure then emits visible
light which might be perceived as ball lightning. The embryonic structure
is visualized in the form of a nucleus having a spatial network structure with
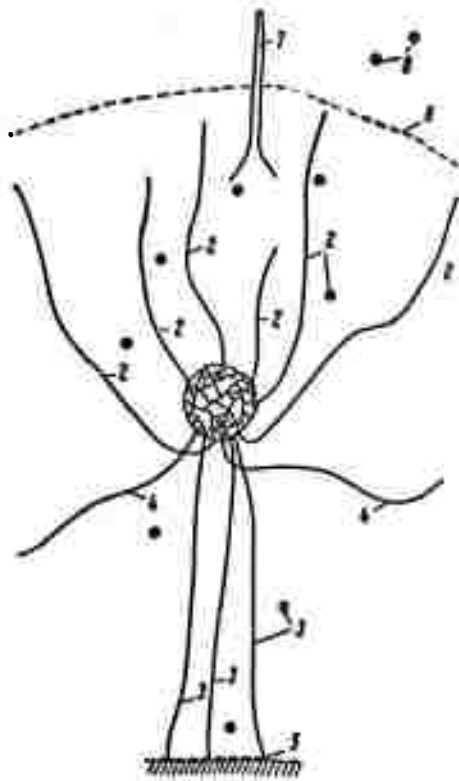spatially interconnected chain structures grown out of it (see Fig. 1). The

Fig. 1. Spatial distribution of ball lightning structures:
1 - spatial network structure and space charge; 2 - upper
structures and space charge; 3 - lower structures and
space charge; 4 - separate ascending lower structure
chains; 5 - lower discharge boundary of lower structures;
6 - upper discharge boundary of upper structures in the
pre-leader discharge phase; 7 - leader channel; 8 - charges
ascending to the cloud.

mechanism of formation of a ball lightning is described on the basis of this model as follows. Discharge currents from separate chains of the upper and lower structures accumulate on the nucleus. Given a sufficient number of chains, of the appropriate length, the total current across a nucleus is able to heat the nucleus structure to the point of visible light emission. At this stage, a quiet luminescence of the nucleus may be observed. A further increase in current across the upper and lower structures results in the accumulation of a significant space charge within the embryonic structures, which periodically forms a short current leader channel of streak lightning. The leader current flows across the embryonic structure. A series of short leaders is perceived by an observer as flashes and explosions of the luminous nucleus. A long leader, resulting from a sudden decrease in structural resistance at the instant of partial burning, is perceived as a strong explosion along with the disappearance of the luminous nucleus. The latter appears to be the ball lightning energy source, although the true source is the static earth-cloud electric field. The leader pumps the field energy from regions at a great distance from the structures. Charged embryonic structures sometimes alternately fall and rise from the ground in a "jumping ball" pattern without breaking away from the earth. This kind of embryo moves only along the earth's surface, subject to the mutually balancing forces of weight and charge attraction by the cloud. In this case the charge of the lower structure breaking contact with the earth is neutralized by the discharge current; the structure falls back to the earth until it is repolarized by the earth-cloud field. The predominance of the charge attraction over the weight of the embryonic structure manifests itself if the structure is heated sufficiently by the dipole discharge current to rise in ascending air streams. In that case, the embryo may be lifted far from the earth.

Optimum conditions for ball lightning formation are a combination of high particle concentration, a strong electric field and high temperature. Such a combination may occur when a layer of ash or soot particles is polarized by a discharge (10^6 - 10^7 v) of streak lightning. The polarized particles form a nucleus which is sintered into a conducting network by corona and arc discharges. The existence of a layer of particles is however not a necessary precondition. The particles may form in an induced discharge channel by partial combustion or vaporization of carbon-containing material or metals. Growth of the upper structures in this case is explained by accumulation after a discharge of the residual particles on the polarized upper part of a spatial structure. A strong electric field created by a current breakdown on the attached particles reestablishes the contact broken by the discharge and promotes growth of the structures. The burned-out spatial structures are recon-

structed from ground material particles by current breaks generated between the spatial structure and earth at the instant of separation from the earth. The particles remaining below the spatial structure after a discharge form the lower structures and close the discharge circuit across the nucleus to the earth. Ball lightning lifetime is limited only by those conditions favorable to structure formation, as long as the nucleus structure is not burned out completely.

Examples are given of other ball lightning characteristics which might be forecast on the basis of the cited mechanism.

Kotenko, V. G., and Yu. A. Litvinenko. Generation of strong pulsed magnetic fields in solenoids of bimetallic wires. ZhTF, no. 1, 1972, 183-186.

The possibility of producing a strong pulsed magnetic field in solenoids has been investigated by using reinforced bimetallic wire as the winding material. One bimetal component forms a highly electrically conductive part, with the other being highly rigid, thus forming a reinforced winding. Experience in using such a winding is outlined. The main design problem is to transfer electrodynamic stress produced in the conducting element to the more rigid part. The degree of loading of the rigid part depends on the construction and the bonding characteristics between the two component metals. Theoretical relationships are derived for determining the amplitude of magnetic field corresponding to the stability limit, and for the tolerable pulse duration of the magnetic field. Computed relationships are reduced to the calculations of a nonreinforced ordinary solenoid, i.e., using only the current-carrying part of the bimetal, so that the basic principle can be applied to any type of reinforcing element. Fig. 1 shows the form of characteristic curves for the relationships obtained.
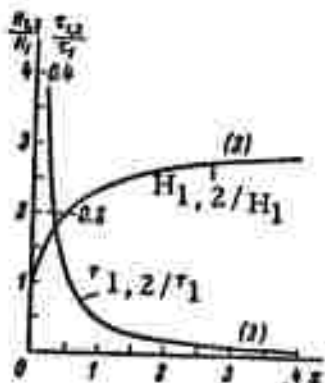

Fig. 1. Design limits of bimetal winding. $H_{1,2}$ - magnetic field corresponding to the stability limit of the reinforced solenoid; H_1 - magnetic field corresponding to the yield point of ordinary nonreinforced solenoid; $x = S_2/S_1$, where S_2 - cross-sectional area of rigid metal and S_1 - cross-sectional area of conducting metal; $\tau_{1,2}$ - pulse duration of magnetic field $H_{1,2}$ and τ_1 - pulse duration of magnetic field H_1

$$\lambda_{1,2} = \lambda_1$$

Experiments were conducted with a NbZrTi (main) - copper (coating) wire, having stability limits $\sigma_{2lim} \approx 200$ kg/mm^2 and $\sigma_1 \approx 20$ kg/mm^2, respectively. At x = 1, the magnetic field can be increased by 2.3 times, while pulse duration decreases by 20 times. Results of experiments using liquid nitrogen and liquid helium along with the calculated results are tabulated (Table 1). The experimental results are in good agreement with the calculated ones, proving the applicability of bimetallic wires for winding materials of a reinforced solenoid.

Cooling	$\tau_{1,2}$ Calculation	$\tau_{1,2}$ Expt	$H_{1,2}$ Calculation	$H_{1,2}^{**}$ Expt	No. of Pulses	Remarks
N	0.3	0.25	460	410	~ 15	} Thermal
He *	0.55	0.25	460	500	~ 10	} destruction of } wires.

Table 1.

* cooling of solenoids lower than liquid hydrogen is not considered.

** voltage of capacitor bank - 4 kv.

From the experimental and calculated results, it may be deduced that use of aluminum as one and steel, tungsten, etc. as the other constituent of the bimetallic wire may make it possible to obtain a relatively long pulse duration of magnetic field on the order of 500~600 koe. A further selection of optimum solenoid forms may increase the magnetic field by an additional 1.2~1.5 times.

Alekseyev, E. I. A description of the interaction of noncoherent radiation with matter. ZhPS, v. 15, no. 6, 1971, 1090-1093.

A general probability expression is presented from which the interaction of radiation with matter can be approximately described. The model assumes most types of noncoherent radiation sources of macro-scopic nature, and includes certain types of laser radiation as well; random noise sources are however excluded. A general expression defining radiation interaction with a density matrix of material elements is given, which can be treated as a system of ordinary stochastic differential equations with stipulated or random initial conditions. A rigorous solution for the assumed model could be obtained by a form of the Fokker-Planck-Kolmogorov equation; however for practical considerations a satisfactory solution may be had by using only the mean value of density matrix elements.

The author illustrates the approach by examples of approximate equations describing differences of population levels in a two-level system, under the effect of radiation taken to be a normal stationary process with zero mean. The method is tedious, requiring computer solution, and is limited to systems with a few levels only, but in theory applies to radiative interaction of arbitrary intensity and spectral characteristic with matter, as long as the radiation may be considered as a normal stationary process.

Askar'yan, G. A., and T. G. Rakhmanina.
Scattering,refraction and reflection of sound
under the action of intense light on a medium.
ZhETF, v. 61, no. 3, 1971, 1199-1202.

An analytical discussion is given describing the effect of powerful optical absorption in a medium on acoustic parameters of that medium. Coherent or noncoherent radiation of sufficient intensity can cause substantial local changes in acoustical scattering, refraction and reflection owing to gas evolution, bubble formation, etc. The case of a liquid medium is treated here, with bubbles assumed to be formed by beam absorption, as this produces drastic changes in the cited acoustical parameters. An expression for mean bubble size is derived as a function of breakdown threshold and other parameters of the liquid medium. A comparison of theoretical scatter in bubbles with scatter in locally heated regions, at the same per unit energy absorption, shows that the bubble scattering cross-section will exceed that of the heated regions by as much as 10^{13}, which indicates the predominant scattering effect of bubble formations. A brief treatment on sound refraction and reflection from optically disturbed regions is also given. The discussion in general is concerned with acoustic velocities ranging from supersonic to hypersonic.